Phenomenological behavior of rock salt: On the influence of laboratory conditions on the dilatancy onset

Ahmed Rouabhi, P. Labaune, M. Tijani, N. Gatelier, G. Hévin

Version of Record: https://www.sciencedirect.com/science/article/pii/S1674775518304323
Manuscript_bb5b8e0171844d5cb08ae6617acc0dd4

Phenomenological behavior of rock salt: On the influence of laboratory conditions on the dilatancy onset

A. Rouabhi[a,*], P. Labaune[a], M. Tijani[a], N. Gatelier[b], G. Hévin[c]

[a] *MINES ParisTech, PSL Research University, Centre de Géosciences, 35 rue St Honoré, 77300 Fontainebleau, France*
[b] *Geostock Entrepose, 2 rue des Martinets, 92500 Rueil-Malmaison, France*
[c] *Storengy, 12 rue Raoul Nordling, 92274 Bois-Colombes, France*

Abstract

Recently, stress-based dilatancy criteria have become essential tools to design underground facilities in salt formations such as gas storage caverns. However, these criteria can depend critically on the volumetric strain measurements used to deduce the dilatancy onset. Results from conventional triaxial compression can show different volumetric behavior depending on the loading conditions, as well as on the measurement techniques. In order to obtain a quantitative understanding of this problem, an experimental program was carried out and the testing procedure was investigated numerically under homogeneous and heterogeneous stress states. The experimental results showed that the deviatoric stress corresponding to the dilatancy onset was significantly dependent on the measurement techniques. With a heterogeneous stress state, the simulation results revealed that the strain measurements at different scales (referred in this paper as local, hybrid or global) can provide different volumetric results with moderate to significant deviations from the idealized behavior, and hence different onset of dilatancy. They also proved that, under low confinement, tensile stresses can take place within the compressed specimen leading to a great deviation of the dilatancy onset from the idealized behavior. From both experimental and numerical investigations, the difference in sensitivity to the measurement techniques between the deviatoric and the volumetric behaviors is explained by the relatively small values of the volumetric strain. The non-ideal laboratory conditions have more impact on this strain than on the deviatoric one. These findings can have implications for the interpretation of the dilatancy behavior

of rock salt, and hence on the geomechanical design aspects in salt formations.

Keywords: Rock salt; Triaxial tests; Dilatancy onset; End restraint; Viscoplasticity

1. Introduction

To design underground facilities in salt formations, an engineering methodology consisting of two successive procedures has emerged during the last few years (e.g. Staudtmeister and Rokahr, 1997; Heusermann et al., 2003; DeVries et al., 2005; Bérest et al., 2008; Sobolik and Ehgartner, 2011; Moghadam et al., 2013, 2015; Ghasemloonia and Butt, 2015; Khaledi et al., 2016; Wang et al., 2016; Yang et al., 2016; Wang et al., 2018a,b): computation of the stress and strain fields using the strain-hardening behavior of rock salt, and then post-processing of the computed results according to some design criteria. Among these criteria are those based on the dilatancy phenomenon corresponding to an irreversible material volume increase under compressive loading (Spiers et al., 1989; Hunsche, 1993; Van Sambeek et al., 1993; Hou, 2003; DeVries et al., 2005; Popp et al., 2012, 2017). At the laboratory scale, this phenomenon is observed during conventional triaxial compression tests when the specimen volume starts decreasing and then increases, without any apparent macroscopic damage. In the stress space, the stress states corresponding to the dilatancy onset define, as in the case of yield and failure criteria, a boundary between the contracting and dilating behaviors of rock salt. Examples of such stress-based dilatancy criteria are given in Fig. 1, where they are represented in the deviatoric stress - mean stress diagram for both compression and extension triaxial tests. Each curve of this figure is called the compressibility/dilatancy boundary or the dilatancy onset boundary (e.g. Cristescu and Hunsche, 1998; Hunsche and Hampel, 1999). However, for a given rock salt, dilatancy onset can depend critically on the experimental data on which they are based. Indeed, in addition to the inevitable bias of specimen variability, many factors may significantly impact the data such as the specimen geometry, the material heterogeneity or the preconditioning of the specimen (DeVries and Mellegard,

*Corresponding author
Email address: ahmed.rouabhi@mines-paristech.fr (A. Rouabhi)

2010; Medina-Cetina and Rechenmacher, 2010), and especially the loading conditions and the measurement techniques.

Concerning the loading conditions, only the effect of the confining pressure (see Fig. 1) and later, the effect of the intermediate principal stress (Hou, 2003; DeVries et al., 2005) have been investigated experimentally, but rare studies have been carried out on the influence of the loading rate, while it is admitted that rock salt exhibits very pronounced time-dependent behavior.

Regarding the measurement techniques, the combination of measurements obtained by different techniques may provide different results, and there is a risk to collect data which do not reflect the true behavior of the material and therefore determine erroneous constitutive properties. This major issue, as will be shown throughout this paper, is particularly important when dealing with the volumetric behavior; the deviatoric behavior is less sensitive to the used techniques. These techniques are ranging from very local techniques, using the smallest strain gauges (Brace et al., 1966), to hybrid techniques, using extensometers of various lengths (DeVries et al., 2005; Ingraham et al., 2014), to global techniques relative to the whole specimen, using the axial displacement between the loading platens and the amount

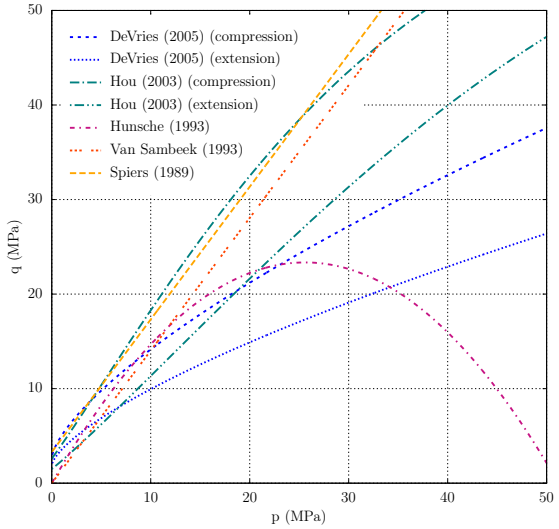

$q = \left[a(\lvert p\rvert/\sigma_0)^n + b\right] \Big/ \left[\cos(\pi/3-\theta) + c\sin(\pi/3-\theta)\right]$
$a = 2.316$ MPa, $n = 0.693$ DeVries et al. (2005)
$b = 2.728$ MPa, $c = 1.066$, $\sigma_0 = 1$ MPa
$q = \eta_D(\sigma_3)\ \beta^{TC}(\sigma_3)\ k_\beta(\sigma_3,\theta)$, $\sigma_3 = -p + (2/3)q\cos(\theta)$
$\eta_D = 1 - a_4\exp(a_5\sigma_3)$, $\beta^{TC} = a_6 - a_7\exp(a_8\sigma_3)$
$k_\beta = \left[\cos(\pi/3-\theta) + a_9\sin(\pi/3-\theta)\right]^{-\exp(a_{10}\sigma_3)}$
$a_4 = 0.8$, $a_5 = 0.055$ MPa^{-1}, $a_6 = 67$ MPa Hou (2003)
$a_6 = 67$ MPa, $a_7 = 41$ MPa, $a_8 = 0.25$ MPa^{-1}
$a_9 = 1$, $a_{10} = 0.25$ MPa^{-1}
$q = ap^2 + bp$
$a = -0.0356$ MPa^{-1}, $b = 1.82$ Hunsche (1993)
$q = ap + b$
$a = 1.4$, $b = 0$ MPa Van Sambeek et al. (1993)
$a = 1.4$, $b = 3.3$ MPa Spiers et al. (1989)
$p = -\operatorname{tr}(\underline{\sigma})/3$, $q = \sqrt{3/2}\lVert\underline{s}'\rVert$, $\theta = \cos^{-1}\left[\sqrt{6}\operatorname{tr}(\underline{J}^3)\right]/3$, $\underline{J} = \underline{s}'/\lVert\underline{s}'\rVert$

Fig. 1. Examples of stress-based dilatancy criteria obtained for different salt rocks plotted in the deviatoric stress - mean stress diagram, and expressed as functions of the three invariants (p, q, θ) of the stress tensor.

of fluid injected or withdrawn from the triaxial cell to maintain a constant confining pressure (Crouch, 1970; Cipullo et al., 1985). Regardless of their global, local or hybrid nature, the obtained measurements are called "axial strain", "radial strain", "volumetric strain", etc., and fitted with constitutive models without further analysis. Using any of these measurements alike implies that stress and strain distributions within the tested specimen are uniform, and thus the laboratory measurements on the boundary of the specimen, whether they are local or not, can directly be compared to the constitutive model predictions.

However, in practice, friction between the loading platens and the specimen ends causes heterogeneities in the stress and strain fields, and an initially perfect right cylinder deforms inevitably into a barrel (triaxial compression) or an hourglass (triaxial extension) shape. As a consequence, different strain measurements may provide different stress-strain curves, and therefore all we can deduce from these curves may be affected by errors which are very difficult to quantify. Different communities in solid mechanics and geotechnical engineering have been studying this issue. Analytical solutions can be found for elastic materials (Brady, 1971; Peng, 1971; Al-Chalabi and Huang, 1974; Chau and Wei, 2000; Wei and Chau, 2009). For more complex behaviors, several numerical studies have been carried out to investigate the effect of different factors on the measured stress-strain curves (Tijani, 1987; Sheng et al., 1997; Ibsen and Lade, 1999; Shilko, 2002; Liyanapathirana et al., 2005; Chemenda, 2015). There are however no studies on volumetric strain and how measurement techniques can affect the measured dilatancy onset.

The main purpose of this paper is to obtain quantitative understanding of the effects of the loading conditions and measurement techniques on the dilatancy onset. Ideally, to investigate this question, it would have been necessary to conduct a detailed experimental program based on a highly instrumented device and including a great variety of testing conditions. However, such a program is very ambitious especially because of the limited number of identical specimens and the required advanced facilities. For this reason, we propose in this work, besides a classical experimental investigation, an extended numerical study. The experimental investigation was conducted to observe the effect of the end restraint and to identify an optimal set of material parameters that correctly reproduces the phenomenolog-

ical observed behavior. The numerical study aims to go further ahead of the experimental analysis, while reducing uncertainties associated with the natural variability of specimens and with the measurement errors.

The paper is organized as follows. Section 2 presents briefly the background behind the volume change during triaxial tests and introduces the definitions of the different types of measurements and the main terms used in the paper. These definitions are used in both experimental and numerical investigations. Section 3 describes the constitutive model that was used in the numerical simulations. Section 4 presents the experimental data and provides the material parameters to be used as input for the simulations. The numerical investigation follows in Section 5. This study is purely mechanical, and the thermal and hydraulic aspects are not considered.

2. Volume change during triaxial tests: Global, local and hybrid measurements

During conventional triaxial tests, the volume change of the specimen can be deduced by combining different types of information, for instance, (i) the global axial displacement between the loading platens, (ii) the amount of fluid displaced into or out of the triaxial cell to monitor the confining pressure, (iii) the global circumferential deformation using a chain extensometer, and (iv) the local measurements using electric resistance strain gauges attached at the mid-height of the lateral surface of the specimen. When the uniformity of the stress and strain fields is ensured, the combination of these different information leads necessarily to equivalent volume change measurement. However, as a consequence of friction that inevitably exists between the loading platens and the specimen ends, the specimen deforms non-uniformly during the test and a distinction between the different combinations becomes essential. This distinction is particularly important in the case of salt rocks, as they generally exhibit small volumetric behavior delicate to measure.

Consider a homogeneous and isotropic cylindrical specimen of radius R_0 and height H_0 subjected, during a conventional triaxial test, to an axial force F and a lateral confining pressure P (see Fig. 2). In a cylindrical coordinate system with unit base vectors $(\overrightarrow{e_r}, \overrightarrow{e_\theta}, \overrightarrow{e_z})$, let the $z-$axis coincide with both the specimen axis and the loading force axis.

The time rate of change of the specimen volume $\mathcal{V}(t)$ can be expressed as

$$\dot{\mathcal{V}} = -\int_{\Omega} \dot{\zeta} \mathrm{d}\mathcal{V} = \int_{\partial\Omega} \overrightarrow{v}.\overrightarrow{n}\mathrm{d}\mathcal{A} \tag{1}$$

with $\dot{\zeta} = -\operatorname{tr}(\underline{\underline{\nabla}}\,\overrightarrow{v})$ the isotropic part of the strain rate tensor $(\underline{\underline{\nabla}}\,\overrightarrow{v})^{\mathrm{S}}$ representing the volume change rate of the material point, where $\overrightarrow{v}$ is the velocity field vector associated with the transformation between the undeformed and deformed configurations of the specimen, and $\overrightarrow{n}$ is the exterior unit normal vector to the specimen boundary $\partial\Omega$. The negative sign is introduced so that contractive strains are positive. According to Eq. (1), the volume change of the specimen can then be calculated by knowing only the movement of its boundary. This can experimentally be achieved by combining the measurements of the global axial displacement and the amount of the displaced confining fluid. Let ζ_{g} denote this global volume change, defined as

$$\zeta_{\mathrm{g}} = -(\mathcal{V} - \mathcal{V}_0)/\mathcal{V}_0 \tag{2}$$

where the subscript g is referring to global.

When using electric resistance strain gauges with small lengths, the local volume change determined by such techniques can be defined as

$$\zeta_{\mathrm{l}} = -(2\varepsilon_\theta + \varepsilon_z) \tag{3}$$

where the subscript l is referring to local; and ε_θ and ε_z are the tangential and axial strains, respectively.

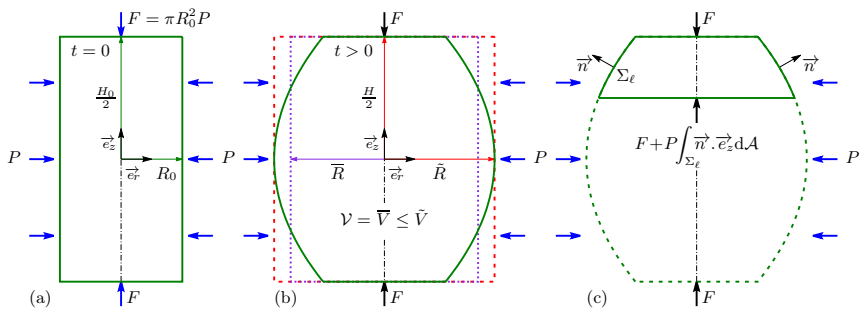

Fig. 2. A sketch of a specimen under triaxial conditions: (a) undeformed configuration, (b) a typical deformed configuration during a triaxial compression, and (c) an illustration of the axial contribution of P.

When the volume change is deduced from the combination of the global axial displacement and a circumferential measure taken around the central part of the specimen, for instance using a chain extensometer or an extended circumferential gauge, this will give rise to an hybrid measurement which, to be directly interpreted, needs the assumption of a particular shape for the deformed specimen. In the case of a cylindrical shape, we can write this hybrid volume change as follows:

$$\zeta_{\mathrm{h}} = -(\mathcal{V} - \tilde{V}_0)/\mathcal{V}_0 = 1 - (1 - \varepsilon_H)(1 + \varepsilon_{\tilde{R}})^2 \tag{4}$$

with

$$\varepsilon_H = -(H - H_0)/H_0, \quad \varepsilon_{\tilde{R}} = (\tilde{R} - R_0)/R_0 \tag{5}$$

where the subscript h is referring to hybrid; $\tilde{R}$ is the radius of the central part of the specimen; $\tilde{V}$ is the volume of the right cylinder with radius $\tilde{R}$ and height H; and ε_H and $\varepsilon_{\tilde{R}}$ are the axial and radial engineering strains (change of length per unit undeformed length), respectively. Remark that, in the particular case when $\varepsilon_H \geq 0$ and $\varepsilon_{\tilde{R}} \geq 0$ (the deformed specimen takes a barrel shape, see Fig. 2b), we have necessarily $\mathcal{V} \leq \tilde{V}$, and hence $\zeta_{\mathrm{g}} \geq \zeta_{\mathrm{h}}$. Furthermore, if we assume that $\varepsilon_H \geq \varepsilon_{\tilde{R}}$ (which is generally the case), we can deduce that $\zeta_{\mathrm{g}} \geq \zeta_{\mathrm{h}} \geq -2\varepsilon_{\tilde{R}} + \varepsilon_H$.

As introduced before, the distinction between the different measurements (global, local and hybrid) is essential only when the specimen deforms non-uniformly during the test. However, when the uniformity is ensured, these strains are equivalent. Indeed, in this case, the strain rate tensor becomes $(\underline{\underline{\nabla}}\, \overrightarrow{v})^{\mathrm{S}} = \dot{L}_\theta(\overrightarrow{e_r} \otimes \overrightarrow{e_r} + \overrightarrow{e_\theta} \otimes \overrightarrow{e_\theta}) + \dot{L}_z \overrightarrow{e_z} \otimes \overrightarrow{e_z}$, with $L_\theta = \ln(R/R_0)$ and $L_z = \ln(H/H_0)$, where R and H are such that $\mathcal{V}/\mathcal{V}_0 = (R/R_0)^2(H/H_0)$. Thus, we can deduce that $\zeta = -(2L_\theta + L_z)$, and then $\mathcal{V} = \mathcal{V}_0 \exp(-\zeta)$. As in our case, ζ is small, unlike the axial and radial strains, we can write $\zeta = -(\mathcal{V} - \mathcal{V}_0)/\mathcal{V}_0$. Consequently, since $\tilde{R} = R$, it follows that $\zeta = \zeta_{\mathrm{h}} = \zeta_{\mathrm{g}}$. The fact that $\zeta = \zeta_{\mathrm{l}}$ comes from the homogeneity of the strain field.

Let us now consider the measured stresses, which unlike strains, are only global. Two kinds of loads are present: the pressure P applied by the confining fluid and the total axial load F acting on the platens. As functions of the Cauchy stress tensor $\underline{\underline{\sigma}}$, they can be defined

as follows:

$$\left.\begin{array}{l} F = -\int_{\Sigma} \underline{\underline{\sigma}}\, \overrightarrow{e_z} \cdot \overrightarrow{e_z} \mathrm{d}\mathcal{A} \\ P = -\underline{\underline{\sigma}}\, \overrightarrow{n} \cdot \overrightarrow{n} \ \left(\text{for } \overrightarrow{x} \in \partial\Omega - \Sigma\right) \end{array}\right\} \tag{6}$$

where Σ is the part of deformed boundary $\partial\Omega$ where F is applied. Thus, due to the lateral deformation of the specimen and the influence of end restraint, the effect of the pressure P over the boundary $\partial\Omega - \Sigma$ is not only radial but also axial at any point of the boundary. Consequently, in a given cross-section of the specimen, the global axial force is known throughout the loading process only if the axial contribution of P is negligible (see Fig. 2c). Moreover, in order to define a global true axial stress consistent with the Cauchy stress concept, that global axial force must be divided by the current cross-sectional area of the specimen. This section can differ significantly from the original area and may be different from one measurement technique to another since it can be deduced either from the lateral strain when dealing with local or hybrid measurements, or from the volumetrically equivalent right circular cylinder when dealing with global measurements.

For simplicity, since in this study our interest is not to characterize the rheological behavior of a particular rock salt, we will assume that the global axial stress, denoted by Q, is simply given by $Q = F/(\pi R_0^2)$. This assumption greatly simplifies our analysis without affecting the results qualitatively, especially because the methodology adopted in this work is basically comparative. With stresses assumed uniformly distributed in the specimen, the Cauchy stress tensor $\underline{\underline{\sigma}}$ can therefore be expressed, in terms of $P > 0$ and $Q > 0$, as follows:

$$\underline{\underline{\sigma}} = -P\underline{\underline{1}} - (Q - P)\overrightarrow{e_z} \otimes \overrightarrow{e_z} \tag{7}$$

In the following we will call the stress difference $|Q-P|$ as the global deviatoric stress, and $(2P+Q)/3$ as the global mean stress. Obviously, these global quantities coincide with their corresponding local stresses $q = \sqrt{3/2}\|\underline{\underline{\sigma}}'\|$ and $p = -\operatorname{tr}(\underline{\underline{\sigma}})/3$ only under the uniformity assumption.

Finally, even if our primary interest is the volumetric response, it is also useful to examine the effect of the different types of measurements on the distortion behavior. Let γ, the work conjugate variable of the deviatoric stress, be the distortion strain. The corresponding local,

hybrid and global measurements can be respectively expressed as

$$\left.\begin{aligned}\gamma_{\mathrm{l}} &= (2/3)|\varepsilon_\theta - \varepsilon_z| \\ \gamma_{\mathrm{h}} &= (2/3)|\ln(1+\varepsilon_{\tilde{R}}) - \ln(1-\varepsilon_H)| \\ \gamma_{\mathrm{g}} &= (2/3)|\ln(1+\varepsilon_{\overline{R}}) - \ln(1-\varepsilon_H)|\end{aligned}\right\} \tag{8}$$

with

$$\varepsilon_{\overline{R}} = (\overline{R} - R_0)/R_0 = \sqrt{(1-\zeta_{\mathrm{g}})/(1-\varepsilon_H)} - 1 \tag{9}$$

where $\overline{R}$ is the radius of the volumetrically equivalent right circular cylinder ($\mathcal{V} = \overline{V}$, see Fig. 2b).

3. Constitutive model

We assume that the material behavior is isotropic during the entire deformation history. This assumption is supported by the fact that the micro-cracking activity associated to the inelastic volume change remains spread out within the volume of the sample, because the occurrence of the macroscopic dilatancy is observed well before any significant macro-crack. We also assume that the strain rate tensor $(\underline{\underline{\nabla}}\,\overrightarrow{v})^{\mathrm{S}}$ can be decomposed into an elastic part and a viscoplastic part denoted by $\underline{\underline{\dot{\varepsilon}}}_{\mathrm{vp}}$. The laws defining $\underline{\underline{\dot{\varepsilon}}}_{\mathrm{vp}}$ are abundant in the literature, since during the last decades, a variety of constitutive models have been devoted to different aspects of rock salt behavior, including more and more physical phenomena, such as transient and stationary creep (e.g. Cristescu, 1993; Munson, 1997; Jin and Cristescu, 1998; Heusermann et al., 2003; Tijani, 2008), tertiary creep (e.g. Chan et al., 1994) or kinematic hardening (e.g. Aubertin et al., 1999).

In this work, we choose to use the recent phenomenological model developed by Labaune et al. (2018) because, besides the fact that it includes dilatancy at the constitutive level, it allows greater flexibility in the depiction of phenomena. It is based on Lemaitre creep model (Tijani, 2008), a commonly used evolution law to describe the viscoplastic behavior of rock salt, and extended to include the effects of the mean stress and the Lode angle. In addition, in order to take into account the tension phenomenon observed during both low-confining-pressure triaxial compression and triaxial extension tests, a tension mechanism of Rankine-type was

added to this model by assuming an additive decomposition of the total strain rate tensor $\dot{\underline{\underline{\varepsilon}}}_{\rm vp}$ into tensile $\dot{\underline{\underline{\varepsilon}}}^{\rm t}_{\rm vp}$ and compressive $\dot{\underline{\underline{\varepsilon}}}^{\rm c}_{\rm vp}$ parts. In what follows we briefly describe the improved version of this model.

The compressive and tensile parts of the viscoplastic strain rate tensor $\dot{\underline{\underline{\varepsilon}}}_{\rm vp}$ are decomposed in the basis $(\underline{I}, \underline{J}, \underline{\underline{K}})$ defined as

$$\underline{I} = \underline{1}/\sqrt{3},\ \ \underline{J} = \underline{\sigma}'/\|\underline{\sigma}'\|,\ \ \underline{\underline{K}} = \left(\sqrt{2}\underline{I} + \ell\underline{J} - \sqrt{6}\underline{J}^2\right)/\sqrt{1-\ell^2} \tag{10}$$

where $\underline{\sigma}'$ is the deviatoric part of the stress tensor; and $\ell = \sqrt{6}\ \mathrm{tr}(\underline{J}^3)$ is the third invariant of $\underline{\sigma}$ which, under triaxial stress conditions, ranges from $\ell = 1$ in triaxial extension to $\ell = -1$ in triaxial compression. When all principal stresses are distinct, the basis $(\underline{I}, \underline{J}, \underline{\underline{K}})$ forms an orthonormal basis for the symmetric second-order tensors that are coaxial with $\underline{\sigma}$.

Under compressive loading, the evolution law of $\dot{\underline{\underline{\varepsilon}}}^{\rm c}_{\rm vp}$ can be written as

$$\dot{\underline{\underline{\varepsilon}}}^{\rm c}_{\rm vp} = -\sqrt{1/3}\dot{\zeta}^{\rm c}_{\rm vp}\underline{I} + \sqrt{3/2}\dot{\gamma}^{\rm c}_{\rm vp}\underline{\underline{N}}^{\rm c} \tag{11}$$

where $\dot{\zeta}_{\rm vp} = -\ \mathrm{tr}(\dot{\underline{\underline{\varepsilon}}}^{\rm c}_{\rm vp})$ and $\dot{\gamma}^{\rm c}_{\rm vp} = \sqrt{2/3}\|\dot{\underline{\underline{\varepsilon}}}^{\rm c\prime}_{\rm vp}\|$ are the rates of the volumetric strain and the viscoplastic distortion, respectively. The unit tensor $\underline{\underline{N}}^{\rm c}$, used to define the deviatoric flow direction, is defined as follows:

$$\underline{\underline{N}}^{\rm c} = \left[\underline{J} - (\varrho'/\varrho)\underline{\underline{K}}\right]\Big/\sqrt{1+(\varrho'/\varrho)^2} \tag{12}$$

where ϱ is a function introduced to account for differences in material behavior between triaxial compression and triaxial extension, with $\varrho'(\theta) = \mathrm{d}\varrho(\theta)/\mathrm{d}\theta$. Its expression as a function of the Lode angle $\theta = \cos^{-1}\ell/3$ is as follows (Bigoni and Piccolroaz, 2004):

$$\varrho(\theta) = \cos\left[\arccos(-\chi)/3\right]\Big/\cos\left\{\arccos\left[\chi\cos(3\theta)\right]/3\right\} \tag{13}$$

where χ is a constant material parameter.

Under tensile loading, the associated strain rate tensor $\dot{\underline{\underline{\varepsilon}}}^{\rm t}_{\rm vp}$ is assumed to be described by a mechanism of Rankine-type:

$$\dot{\underline{\underline{\varepsilon}}}^{\rm t}_{\rm vp} = \dot{\lambda}\frac{\partial G}{\partial \underline{\underline{\sigma}}} \tag{14}$$

with

$$G = \left(\langle \sigma_1 \rangle^d + \langle \sigma_2 \rangle^d + \langle \sigma_3 \rangle^d \right)^{(1/d)} \tag{15}$$

where $\dot{\lambda}$ is a positive multiplier; $\langle \cdot \rangle$ are the Macaulay brackets, i.e. $\langle x \rangle = (x + |x|)/2$; $\sigma_1 \geq \sigma_2 \geq \sigma_3$ are the principal stresses of $\underline{\underline{\sigma}}$; and $d \geq 1$ is a constant parameter that determines the shape of the potential surface between the two limit cases of $d = 1$ and $d \to +\infty$. The function G, used by Chaboche et al. (1994) and Carol et al. (2001) to model the damage of brittle materials, is differentiable for all stress states which reduce the numerical difficulties associated with the gradient calculation. When d tends to infinity, it approaches a Rankine-type model ($G = \sigma_1$).

When the gradient of G with respect to $\underline{\underline{\sigma}}$ is written in the basis ($\underline{\underline{I}}$, $\underline{\underline{J}}$, $\underline{\underline{K}}$), for consistency with the compressive part of the model, Eq. (14) can be rewritten as

$$\dot{\underline{\underline{\varepsilon}}}^{\mathrm{t}}_{\mathrm{vp}} = -\sqrt{1/3}\dot{\zeta}^{\mathrm{t}}_{\mathrm{vp}}\underline{\underline{I}} + \sqrt{3/2}\dot{\gamma}^{\mathrm{t}}_{\mathrm{vp}}\underline{\underline{N}}^{\mathrm{t}} \tag{16}$$

with

$$\dot{\zeta}^{\mathrm{t}}_{\mathrm{vp}} = -\dot{\lambda}X, \;\; \dot{\gamma}^{\mathrm{t}}_{\mathrm{vp}} = \dot{\lambda}\sqrt{Y^2 + Z^2} \tag{17}$$

where the deviatoric tensor $\underline{\underline{N}}^{\mathrm{t}}$ and the quantities X, Y and Z are such that

$$\left.\begin{aligned} \underline{\underline{N}}^{\mathrm{t}} &= \left[(Y\cos\theta + Z\sin\theta)\underline{\underline{J}} + (Z\cos\theta - Y\sin\theta)\underline{\underline{K}} \right] \Big/ \sqrt{Y^2 + Z^2} \\ X &= G'_1 + G'_2 + G'_3 \\ Y &= (2G'_1 - G'_2 - G'_3)/3 \\ Z &= (G'_2 - G'_3)/\sqrt{3} \end{aligned}\right\} \tag{18}$$

and $G'_i = \langle \sigma_i / G \rangle^{d-1}$ are the principal values of $\partial G / \partial \underline{\underline{\sigma}}$.

Finally, the additive decomposition of the total strain rate tensor $\dot{\underline{\underline{\varepsilon}}}_{\mathrm{vp}}$ into tensile $\dot{\underline{\underline{\varepsilon}}}^{\mathrm{t}}_{\mathrm{vp}}$ and compressive $\dot{\underline{\underline{\varepsilon}}}^{\mathrm{c}}_{\mathrm{vp}}$ parts, leads to

$$\dot{\underline{\underline{\varepsilon}}}_{\mathrm{vp}} = -\sqrt{1/3}\dot{\zeta}_{\mathrm{vp}}\underline{\underline{I}} + \sqrt{3/2}\left(\dot{\gamma}^{\mathrm{c}}_{\mathrm{vp}}\underline{\underline{N}}^{\mathrm{c}} + \dot{\gamma}^{\mathrm{t}}_{\mathrm{vp}}\underline{\underline{N}}^{\mathrm{t}} \right) \tag{19}$$

with $\dot{\zeta}_{\mathrm{vp}} = \dot{\zeta}^{\mathrm{c}}_{\mathrm{vp}} + \dot{\zeta}^{\mathrm{t}}_{\mathrm{vp}}$. As can be seen from this equation, the tensile contribution acts on both components of $\dot{\underline{\underline{\varepsilon}}}_{\mathrm{vp}}$, volumetric and deviatoric.

To fully define $\dot{\underline{\underline{\varepsilon}}}_{\mathrm{vp}}$, the variables $\dot{\gamma}^{\mathrm{c}}_{\mathrm{vp}}$, $\dot{\zeta}^{\mathrm{c}}_{\mathrm{vp}}$ and $\dot{\lambda}$ still need to be defined, which will be done as follows.

For the compressive part, the evolution law of $\zeta^{\mathrm{c}}_{\mathrm{vp}}$ is expressed as

$$\dot{\zeta}^{\mathrm{c}}_{\mathrm{vp}} = \psi(\underline{\underline{\sigma}}, \gamma^{\mathrm{c}}_{\mathrm{vp}})\dot{\gamma}^{\mathrm{c}}_{\mathrm{vp}} \tag{20}$$

with

$$\psi(\underline{\underline{\sigma}}, \gamma^{\mathrm{c}}_{\mathrm{vp}}) = v\frac{\langle p/N\rangle^n - \gamma^{\mathrm{c}}_{\mathrm{vp}}}{\langle p/M\rangle^m + \gamma^{\mathrm{c}}_{\mathrm{vp}}} \tag{21}$$

and that corresponding to $\gamma^{\mathrm{c}}_{\mathrm{vp}}$ is given through a generalization of Lemaitre model, enriched with an influence of the mean pressure p and the Lode angle θ:

$$\frac{\mathrm{d}(\gamma^{\mathrm{c}}_{\mathrm{vp}})^{1/a}}{\mathrm{d}t} = \Big\langle \Big[q/\varrho(\theta) - (\gamma^{\mathrm{c}}_{\mathrm{vp}})^b Bp - C\Big]/K \Big\rangle^{k/a} \tag{22}$$

In Eq. (21), the sign of $\langle p/N\rangle^n - \gamma^{\mathrm{c}}_{\mathrm{vp}}$ indicates whether the behavior is contracting or dilating.

Regarding the tensile part, we consider an evolution law of Perzyna-type:

$$\dot{\lambda} = \Lambda \Big\langle \Big(G - R_{\mathrm{t}}\Big)/S \Big\rangle^s \tag{23}$$

In Eqs. (21)-(23), v, n, m, a, b, B, C, k, Λ, R_{t}, s, M, N, K and S are the material parameters. The moduli M, N, K and S may depend on the thermodynamic state to represent the effects of temperature, softening or other phenomena. However, in this study, they are assumed to remain constant.

4. Experimental data and material parameters

We present some typical results obtained from an experimental campaign conducted on a rock salt cylindrical specimens with a diameter of 65 mm and a height of 130 mm. The specimens were obtained from core samples taken at a depth of nearly 1330 m in a salt dome situated in the Landes region of the southwest of France. The geological description indicated that those specimens are halite salt with a content of insoluble materials lying between 4% and 7%. The results for nine of the performed tests are presented in this

section: two short-term uniaxial tests, six short-term triaxial tests with three different levels of confining pressure (5 MPa, 10 MPa and 15 MPa), and one creep test at constant confining pressure (5 MPa) with three stages of the deviatoric stress (5 MPa, 10 MPa and 15 MPa). All of them were conducted at room temperature (22 °C). Each test includes an isotropic phase during which the specimen is loaded hydrostatically to the target pressure, followed by a deviatoric phase during which the confining pressure is held constant and the global axial stress is increased. Only the deviatoric phase is analyzed in this work. Any irreversible damage caused during the isotropic phase is thus neglected; this assumption is generally accepted by most of the literature on rock materials (Ulusay, 2015).

Short-term tests were loaded axially by a servo-hydraulic material test system (MTS) under a constant strain rate of 5×10^{-6} s^{-1}. Confined tests were performed in a triaxial cell capable of supporting up to 20 MPa of confining pressure and regulated by a pressure/volume controller. During the tests, each specimen was submitted to three loading-unloading cycles in order to ensure, on one hand, the right behavior of gauges and, on the other hand, the accurate determination thereafter of the elastic parameters. The local axial and circumferential strains were measured by strain gauges attached at the mid-height of each specimen. The global axial displacement was measured by means of a linear variable differential transducer (LVDT) sensor. The global volume change of the confined tests was measured from the volume change of the confining fluid. For these tests, hybrid measurements using a circumferential chain extensometer were difficult to obtain without degrading the sensitivity of the global volume measurements since, with this technique, larger confining cells are needed and therefore the volume of the confining fluid is more important. Neither hybrid nor global measurements were exploited for the unconfined tests.

The multistage creep test was carried out during a period of 45 d in a triaxial cell and submitted to an axial and a lateral pressures applied by a pressurized oil system. Neither local strain nor global volume change was measured. The global axial displacement was measured with an LVDT sensor as for the short-term tests.

Experimental results and model response of all tests are shown in Figs. 3-7. Each figure includes experimental strains measured with one or two different methods. Fig. 3 shows the

uniaxial short-term tests; Figs. 4-6 show the short-term tests with the confining pressures of 5 MPa, 10 MPa and 15 MPa, respectively; Fig. 7 shows the long-term creep test. For the short-term tests, the stress-strain responses are presented in two graphs showing the global deviatoric stress versus the volumetric strain on the left, and the global deviatoric stress versus the distortion strain on the right. For the long-term test, the global axial strain as well as the global deviatoric stress is plotted as a function of time.

Figs. 3-7 also include the model response obtained through a global fitting procedure based on the global measurements of all the collected data (global-global fitting), and on the assumption of uniformity of the stress and strain fields. This fitting procedure was performed as follows. The elastic parameters (Young's modulus E, and Poisson's ratio ν) were fitted using the loading-unloading cycles of the short-term triaxial tests. Then the other parameters were fitted in two steps: the parameters related to distortion by fitting γ^{c}_{vp} (evolution law Eq. 22), and the parameters related to dilatancy by fitting ζ^{c}_{vp} (evolution law Eq. 20). It is important to note that since the expression of ζ^{c}_{vp} depends on γ^{c}_{vp}, it can be fitted in two different ways: using the previously-fitted values for γ^{c}_{vp}, or the experimental values. In this study, we decided to use the experimental values to ensure the independence of the two steps. All the fittings were performed using an error minimization procedure based on the least square method. The fitted parameters are listed in Table 1. Since the stress state was compressive during all the tests, the parameters related to the Lode angle dependency (Eq. 13) as well as those related to the tension mechanism (Eq. 23) were not fitted. They were considered in the following numerical simulations as arbitrary constants that will be fixed through parametric investigations.

Several conclusions can be drawn from those figures. First, we can see that the volumetric behavior is critically dependent on the used measurement techniques, unlike the deviatoric behavior where the difference between local and global measurements is rather limited and may remain within the experimental error limits. It is well known that strain gauges measures could be misleading due to highly localized deformations but, in our case, no strain localization phenomena were observed and dilatancy occurred without any significant apparent damage. Moreover, if we judge their behavior based on the loading-unloading

cycles during the whole duration of each test, they seem to behave rather correctly since the rigidity is substantially the same for the different cycles. Thus, the difference between local and global measurements cannot be associated only with gauge dysfunctions.

Second, for a given confining pressure, the variation from one specimen to another seems to have a more significant effect on the volumetric response than on the deviatoric response, especially when considering the local measurements. Any information deduced from the volumetric response is thus impacted by both the used measurement techniques and the specimen variability. The numerical study presented thereafter allows to set aside the natural variability and study only the question of uncertainties associated with the type of the measurement techniques.

Third, based on the obtained measurements for the confined tests, it seems that the onset of the dilatancy phenomenon, which can be deduced from the sign change of the inelastic volumetric strain rate, occurs for relatively small volumetric strains; the maximum value is around 0.17%, obtained by the global measurements for the highest confining pressure of 15 MPa. Therefore, the difference in sensitivity to the measurement techniques between the deviatoric and the volumetric behaviors can be explained by the fact that the strain volumetric component is relatively small, and consequently it is more affected by the non-ideal laboratory conditions than the deviatoric component. Notice that the small values of the volumetric strains are not only specific to the present study but also characterize rock salt in general. This explains why in practical applications the strain volumetric component was often ignored in favor of the deviatoric component, especially in the case of salt cavern creep problems.

Fourth, we can notice that the model is capable of simultaneously fitting all the experimental data with the same parameter set. Obviously, a better fit could be obtained by considering individual tests but it would give rise to different parameter sets. Remark that model results for the unconfined tests are in much more disagreement with the local measurements than those for confined tests, not only in terms of the volumetric behavior, but also in terms of the deviatoric behavior. It is generally accepted that results of unconfined and low confined tests are less reliable than those of high confined tests, but since

no quantitative arguments can be advanced to explain their unreliability and inaccuracy, it is then difficult to quantify the disagreement between the model and the measurements. Under low confinement pressure, the friction between the platens and the specimen ends seems to cause tensile stresses, as we shall show in the numerical investigations (Section 5), which may explain this disagreement between the model, which assumes uniform and only compressive stress state, and the measurements.

In the determination of the material parameters of Table 1, it has been assumed that the strain and stress states are homogeneous in the specimen but, as might be deduced from the difference between local and global measurements, it is highly probable that these distributions were heterogeneous during the actual tests. Hence, by no means those parameters values could be considered as intrinsic material properties which can be used directly in the constitutive laws. The best way to better interpret the experimental results is to use a numerical fitting process that considers the tested specimen as an instrumented structure subjected to boundary conditions; those determined parameters values might then be used as starting values for this process. However, as in this work the main focus is not the accurate characterization of a particular rock salt as already mentioned above, we will use in the following sections the material parameters of Table 1 since they can correctly reproduce the phenomenological observed behavior, whether it is volumetric or deviatoric.

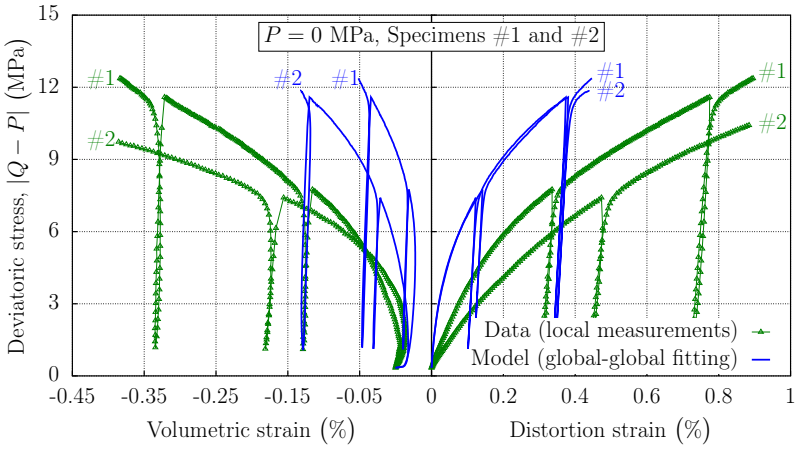

Fig. 3. Measured stress-strain curves for uniaxial compression tests, compared with the global-global fitting.

Table 1

Rock salt material constants.

Parameter		Unit	Value
Elastic	E	MPa	$27,610$
	ν		0.32
Eq. (21)	v		0.256
	n		0.972
	N	MPa $(\mu\text{m}^{-1}\ \text{m})^{1/n}$	0.0012
	m		2.378
	M	MPa $(\mu\text{m}^{-1}\ \text{m})^{1/m}$	0.334
Eq. (22)	a		0.29
	b		0.24
	B	$(\mu\text{m}^{-1}\ \text{m})^{b}$	0.044
	C	MPa	0
	k		2.2
	K	MPa $(\mu\text{m}^{-1}\ \text{m}\ \text{d}^{a})^{1/k}$	0.128
	χ		0
Eq. (23)	R_t	MPa	0
	S	MPa	0.1
	s		0.25
	d		10
	Λ	$\mu\text{m}\ \text{m}^{-1}\ \text{d}^{-1}$	0

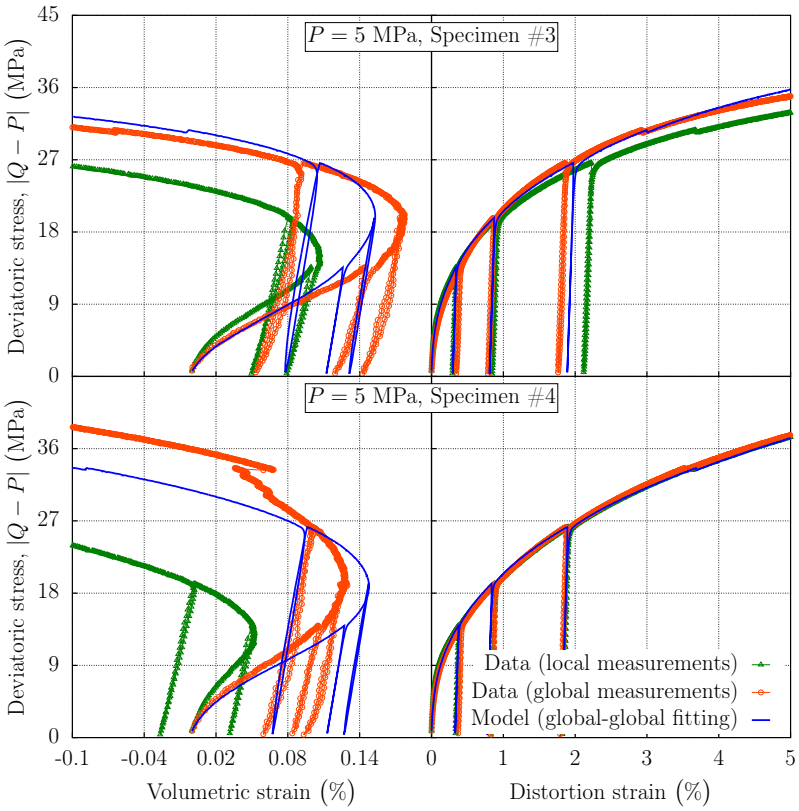

Fig. 4. Measured stress-strain curves for triaxial compression tests under confining pressure $P = 5$ MPa, compared with the global-global fitting.

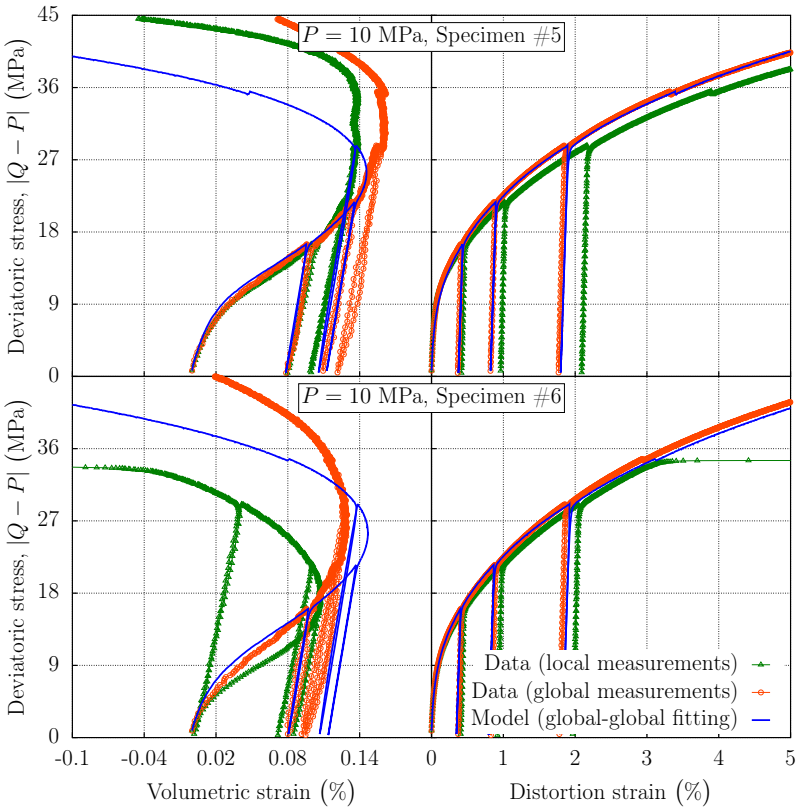

Fig. 5. Measured stress-strain curves for triaxial compression tests under confining pressure $P = 10$ MPa, compared with the global-global fitting.

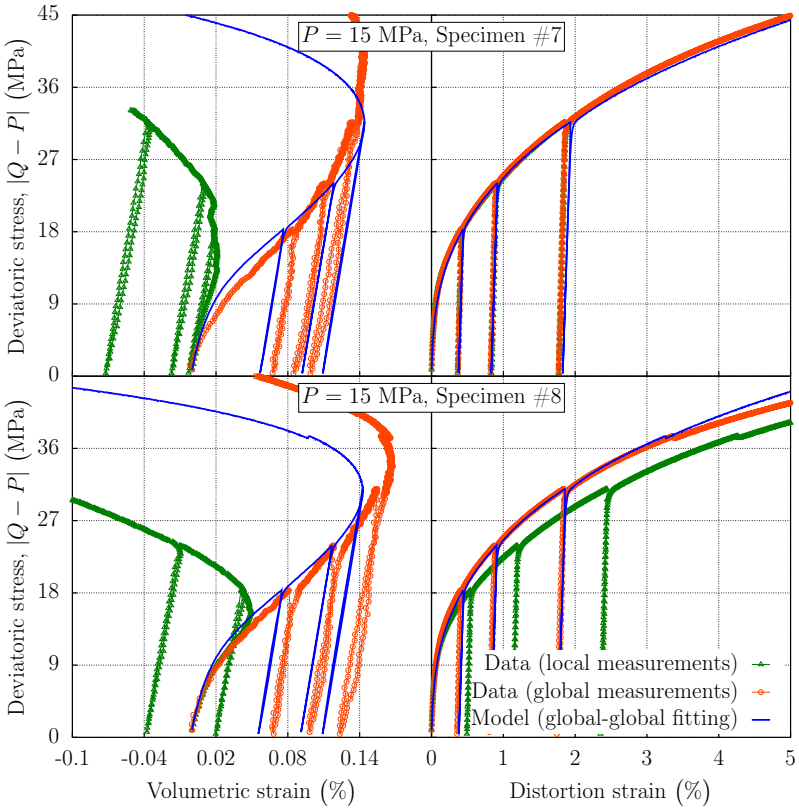

Fig. 6. Measured stress-strain curves for triaxial compression tests under confining pressure $P = 15$ MPa, compared with the global-global fitting.

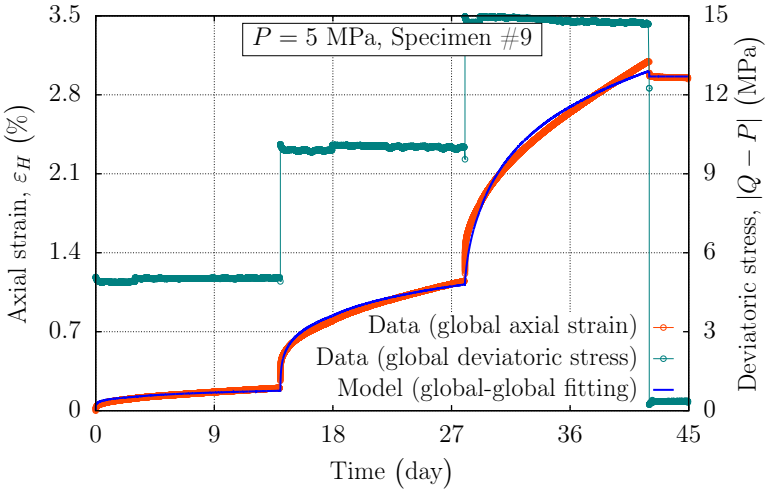

Fig. 7. Measured creep axial strain versus time under three deviatoric stresses (5 MPa, 10 MPa and 15 MPa), compared with the global-global fitting.

5. Numerical investigation

The objective of the numerical simulations is to obtain a quantitative understanding on how the measurement techniques, the loading rate, the confining pressure and the intermediate principal stress can influence the dilatancy onset and the stress spatial distribution within the specimen at the time for which this onset is observed. A summary of the main results is given in Section 5.5.

All numerical simulations were carried out within the large deformation framework using the finite element code VIPLEF developed by MINES ParisTech (Tijani, 1996). In this code, large strain computations are taken into account by using the updated Lagrangian approach (Fung and Tong, 2001) which consists of decomposing the body motion into small steps and by updating the body geometry as well as the stress state. The principal reason to consider such a framework is to take into account the finite geometry changes during the loading process in order to accurately calculate the specimen volume. Since the volume change is rather small (less than 0.2% in the present study), the error associated with the small strain assumption indeed greatly impacts the volume change calculation.

In those simulations, our attention was restricted to the two extreme conditions of specimen-platen contact: smooth contact where there is no friction between the specimen and the loading platens (ideal case representing the idealized testing conditions), and rough contact where there is a complete radial restraint at the specimen ends. Since the simulated specimen and loads were symmetric with respect to the $z-$axis, only a quarter of the specimen was simulated. A uniform mesh with 2000 nine-node quadrilateral elements was used in the case with rough contact. Only one nine-node quadrilateral element was used in the case of smooth contact because the stresses and strains are uniform throughout the specimen.

The constitutive model of Section 3 was implemented in VIPLEF and the model parameters were taken from Table 1. The parameters χ and Λ that control the Lode angle dependency and the tensile behavior, respectively, may vary between the following numerical simulations: the value of each of them is either zero (reference value) or given in the captions

of the figures showing the corresponding numerical results. Parameters R_{t}, S and s, useful only when Λ is non-zero, are kept constant and their values are equal to the reference values given in Table 1.

As in the experimental case, the initial conditions are taken to correspond to the end of the isotropic phase. Concerning the boundary conditions, two types of boundary conditions are investigated. The first one corresponds to triaxial compression tests (constant axial strain rate $\dot{\varepsilon}_H$ and constant confining pressure P). The second one, chosen to study the effects of the intermediate principal stress, corresponds to triaxial extension tests (constant axial stress rate $\dot{Q}$ and constant confining pressure rate $\dot{P}$). To simplify the notations, in the following we refer to these conditions as strain- and stress-controlled, respectively.

The principal numerical results are of two types: those representing the stress-strain curves and those representing, at fixed times, the spatial distribution of some variables of interest.

The former results, which are interpreted numerically in a manner similar to the interpretation of laboratory measurements, are systematically given for the three types of measurements considered in this paper: local, hybrid and global, and for both types of specimen-platen contacts: smooth and rough. In each case, given that we focus on the influence of the laboratory conditions on the dilatancy onset, the deviatoric stress corresponding to this onset is indicated (horizontal dashed lines) in the global deviatoric stress - volumetric strain diagram. This deviatoric stress, referred in what follows as the dilatancy deviatoric stress, is calculated according to the formula $\mathrm{d}\zeta_{\mathrm{vp}}/\mathrm{d}|Q-P| = 0$, which determines the dilatancy onset as the maximum of the volumetric viscoplastic strain with respect to the global deviatoric stress. In the case of the smooth contact (homogeneous stress state), all the curves coincide completely with each other and the condition corresponding to the dilatancy onset is equivalent to $\dot{\zeta}_{\mathrm{vp}} = 0$. In this case, those curves are indicated using a bar over the variable, such as $\overline{\zeta}$ or $\overline{\gamma}$, and the dilatancy deviatoric stress is denoted by $\overline{q}^{\star}$.

Regarding the spatial distributions, the results concern the contour maps either of the major principal stress σ_1 or of the function $\hat{\varphi}$ defined by $\hat{\varphi} = (1 - \varphi/\overline{\varphi}) \times 100$, where φ and $\overline{\varphi}$ are the functions associated with the deformed specimen with and without end

restraint, respectively. The function $\hat{\varphi}$, representing in this study one of the three invariants $\hat{p}$, $\hat{q}$ and $\hat{\ell}$, defines a relative deviation from the ideal situation. The time at which those spatial distributions are plotted is the time $t^\star$ corresponding to $\dot{\bar{\zeta}}_{\mathrm{vp}} = 0$ in the ideal case, unless otherwise indicated. All contours are plotted on the deformed specimen where the displacement is scaled uniformly by a factor A (values specified in the caption of the figures) in order to amplify the deformation. Moreover, to better separate negative from positive contours, all results are plotted on the upper half of the specimen with negative values on the left and positive values on the right. For comparison purposes, the geometry of the deformed specimen without end restraint as well as the initial geometry is also added to these plots.

5.1. Measurement technique effects

In these investigations, the axial strain rate $\dot{\varepsilon}_H$ is fixed to 10^{-5} s^{-1} and the confining pressure P is fixed to 10 MPa.

Fig. 8 shows the stress-strain curves obtained using the parameters of Table 1. As expected for the deviatoric behavior, the different numerical measurements remain relatively close to one another and respect the fact that the local and global measurements are the closest and the farthest to the ideal case, respectively. The hybrid measurements are situated between these two extremes. Overall, the differences between the local and global measurements are in the same order of magnitude as those arising from experimental data. In contrast, for the volumetric behavior, the numerical measurements are quite different from each other especially the hybrid ones, the ideal case is situated between the local and global measurements, and the differences between these measurements are clearly less important than those arising from experimental data.

The observed differences in the volumetric stress-strain curves have a direct impact on the global dilatancy deviatoric stress (represented by the horizontal dashed lines in Fig. 8). Compared to the ideal case ($\approx$ 27 MPa), the dilatancy deviatoric stress is overestimated by the global measurements ($\approx$ 29 MPa), while it is underestimated by local measurements ($\approx$ 25 MPa); the worst scenario is given by the hybrid measurements ($\approx$ 16 MPa).

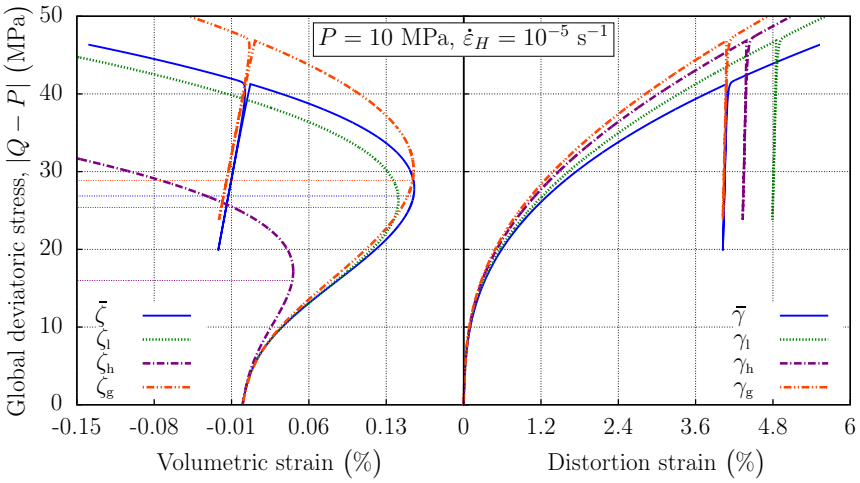

Fig. 8. Numerical stress-strain curves for a triaxial compression test.

5.2. Loading rate effects

In these investigations, the confining pressure P is fixed to 10 MPa and the numerical tests are carried out for different axial strain rates $\dot{\varepsilon}_H$.

Fig. 9 shows the deviatoric stress $\bar{q}^\star$ (normalized by its value $\bar{q}^{\star\star}$, obtained for $\dot{\varepsilon}_H = 10^{-5}$ s $^{-1}$) as a function of the axial engineering strain rate $\dot{\varepsilon}_H$ for a range between 10^{-7} s $^{-1}$ and 10^{-4} s $^{-1}$. From this figure, it is clear that the dilatancy deviatoric stress increases significantly with the loading rate, by nearly 40% in the range between 5×10^{-6} s $^{-1}$ and 5×10^{-5} s $^{-1}$ generally found in laboratory testing programs.

Regarding the case with end restraint, Fig. 10 shows, at the time $t^\star$, the contour maps of $\hat{q}$ for three different strain rates $\dot{\varepsilon}_H$. As can be observed from this figure, for the case with rough contact, the deformation of the specimen in a barrel-shape induces a large deviation from the ideal case. Close to the interface between the specimen ends and platens, the deviatoric stress q is excessively overestimated, whereas it is underestimated elsewhere, with a maximum value around 15 % at a distance of about $H/4$ from the end surface. Under the considered strain rates, the material's viscosity seems however to have only a slight influence on the spatial distribution of $\hat{q}$ as can also be deduced from Fig. 10.

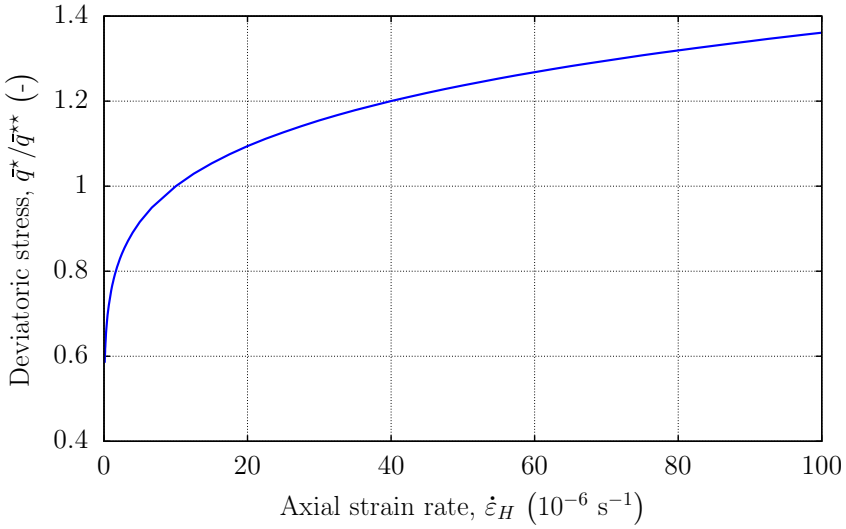

Fig. 9. Effect of the loading rate on the dilatancy deviatoric stress in the ideal case.

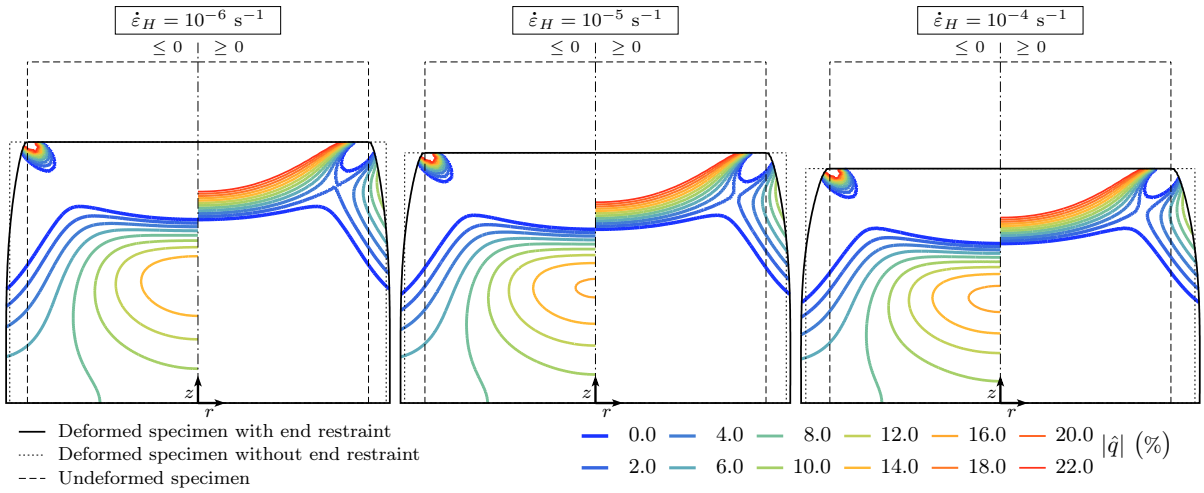

Fig. 10. Contour maps of the relative variation $\hat{q}$ for three loading rates, with displacement scaling factor $A = 20$.

5.3. Confining pressure effects

In these investigations, the axial strain rate $\dot{\varepsilon}_H$ is fixed to 10^{-5} s^{-1} and the numerical tests are carried out for different confining pressures P.

Fig. 11 shows, for the ideal case, the deviatoric stress $\bar{q}^\star$ (normalized by its value $\bar{q}^{\star\star}$, obtained for $P = 10$ MPa) as a function of the confining pressure P. As expected from the formulation of the constitutive model and in accordance qualitatively with the data of

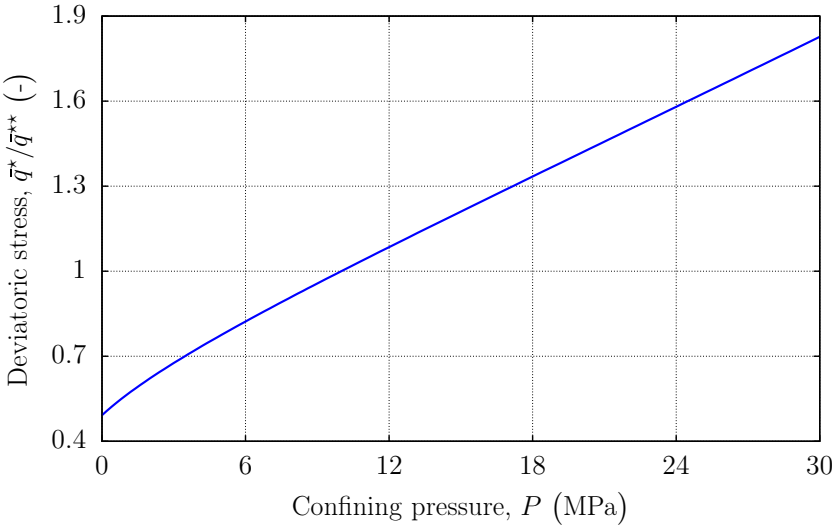

Fig. 11. Effect of the confining pressure on the dilatancy deviatoric stress in the ideal case.

Fig. 1, the dilatancy deviatoric stress $\bar{q}^\star$ increases with the confining pressure, and hence with the mean pressure.

Regarding the case with end restraint, we shall distinguish in what follows between low confining pressure and high confining pressure. In fact, the end restraint may cause the major principal stress to deviate from the compressive regime, depending on the value of the confining pressure.

5.3.1. Low confining pressure

Fig. 12 shows, at the time $t^\star$, the contour maps of σ_1 for the unconfined case ($P = 0$ MPa) and for two low confining pressures P (0.2 MPa and 0.5 MPa), knowing that the authors are aware that very low confining pressures are experimentally difficult to handle but were only studied in order to understand the effects of the presence of tensile zones on the dilatancy deviatoric stress. As can be seen, with rough contact, the heterogeneity of the stress field induces tensile zones ($\sigma_1 > 0$) inside the specimen whose extent decreases as the confining pressure increases.

When the tension mechanism is ignored ($\Lambda = 0$), the stress-strain curves are qualitatively similar to those of Fig. 8. However, they can greatly differ when that mechanism is activated.

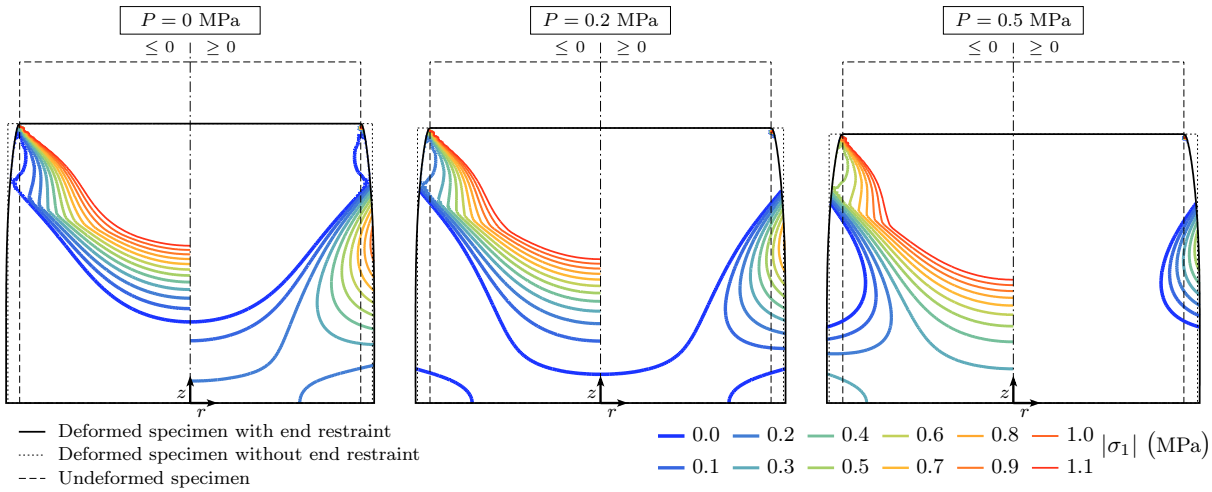

Fig. 12. Contour maps of the major principal stress σ_1 (tension positive) for three low confining pressures, with displacement scaling factor $A = 50$.

Fig. 13 shows a typical result obtained for an unconfined test using the parameters of Table 1, except parameter Λ which is given in the caption of Fig. 13. As we can see, this might suggest, especially when omitting the global method since it cannot be experimentally used in this case, that the condition of homogeneity is satisfied (local and hybrid measurements coincide), while in fact the real stress field in the specimen is far from uniform and the true dilatancy deviatoric stress is widely underestimated ($\approx$ 5 MPa instead of 13 MPa). Note that the activation of the tension mechanism has no significant effect on the deviatoric behavior. It is also worth noting that the parameter R_t in the tension mechanism (Eq. (23)) is assumed to be equal to zero which is consistent with the compression mechanism (the parameter C in Eq. (23), representing the cohesion, was found to be effectively zero) and with the fact that rock salt is very often considered without any intrinsic cohesion (e.g. Tijani, 2008).

5.3.2. High confining pressure

Due to the previous investigations, it was deduced that, once the confining pressure exceeds a few MPa, about 1 MPa in the case treated in this paper, the major principal stress within the specimen remains always negative, thereby enabling only the compression

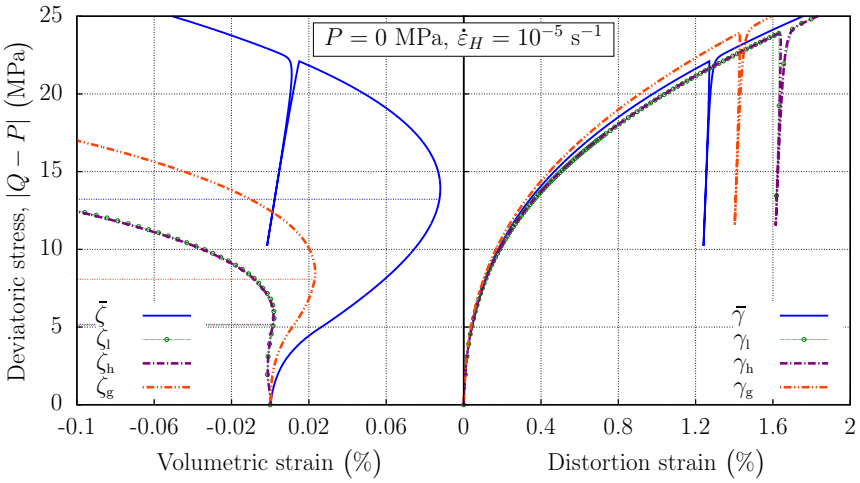

Fig. 13. Numerical stress-strain curves for an uniaxial compression test, with tensile multiplier $\Lambda = 10^6$.

mechanism.

Figs. 14-16 show the contour maps of the relative variations $\hat{p}$, $\hat{q}$ and $\hat{\ell}$ corresponding respectively to the three invariants p, q and ℓ, for three confining pressures (5 MPa, 10 MPa and 15 MPa). As can be observed from these figures, the confining pressure value does not really influence the stress field distribution within the specimen. In contrast, for a given confining pressure value, the end restraint seems to significantly influence this distribution, especially the first and the second invariants p and q; the third invariant ℓ for its part remains, except in a small zone close to the specimen-platen interface, relatively close to the ideal case which corresponds in this case to $\bar{\ell} = -1$.

5.4. Intermediate principal stress effects

To assess the effect of the intermediate principal stress, we investigate in this section stress-controlled numerical tests based on constant global mean pressure $(2P + Q)/3$ rather than on constant confining pressure P. This choice is motivated by the fact that such tests are recently used in the literature to study in particular the dilatational behavior of rock salt (e.g. DeVries et al., 2005; Mellegard et al., 2005) since, in this case, the determination of the dilatancy deviatoric stress, under the assumption of homogeneous stress field, is straightforward. Practically, to keep the global mean pressure constant during the deviatoric

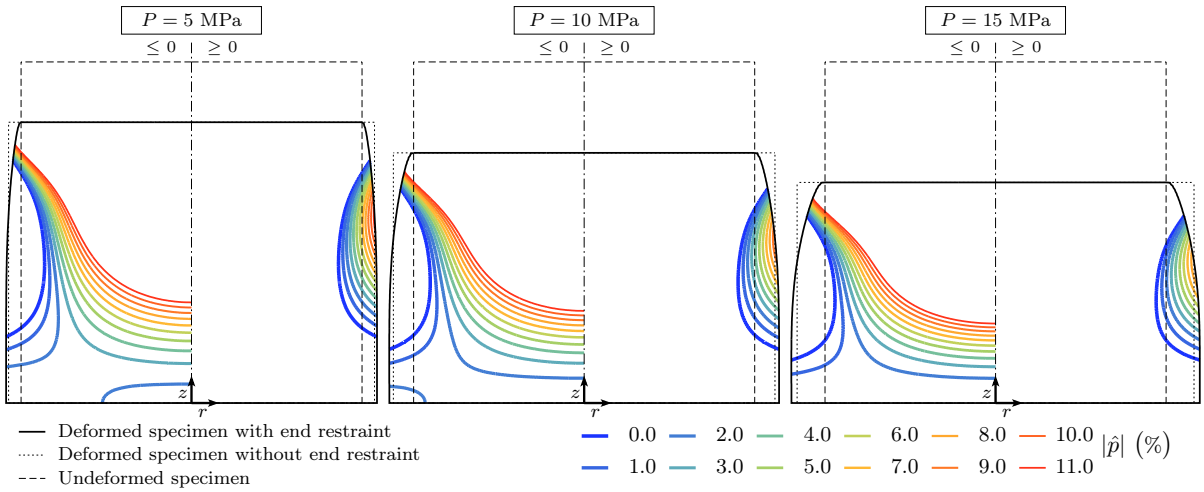

Fig. 14. Contour maps of the relative variation $\hat{p}$ for three confining pressures, with displacement scaling factor $A = 20$.

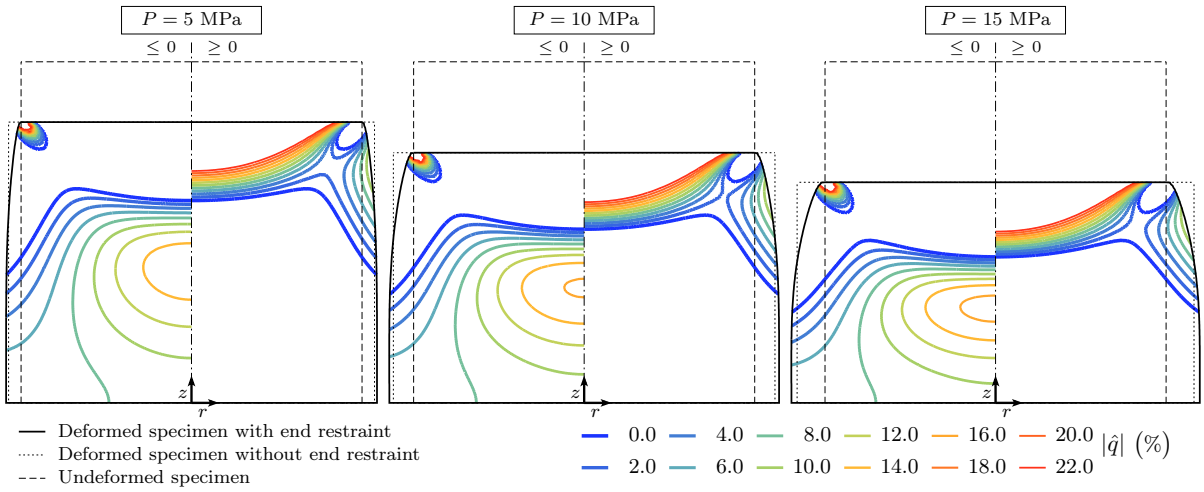

Fig. 15. Contour maps of the relative variation $\hat{q}$ for three confining pressures, with displacement scaling factor $A = 20$.

phase, the rates $\dot{Q}$ and $\dot{P}$ of respectively the axial and the lateral pressures are applied such that $2\dot{P} + \dot{Q} = 0$. Tests are terminated when one of the pressures reaches zero.

In these investigations, the axial pressure rate $|\dot{Q}|$ and the global mean pressure $(2P + Q)/3$ are fixed to 10 MPa/d and 15 MPa, respectively. The global mean pressure value is selected such that neither of the loading pressures reaches zero before the dilatancy onset.

As in the previous sections, we begin our analysis by first investigating the model's

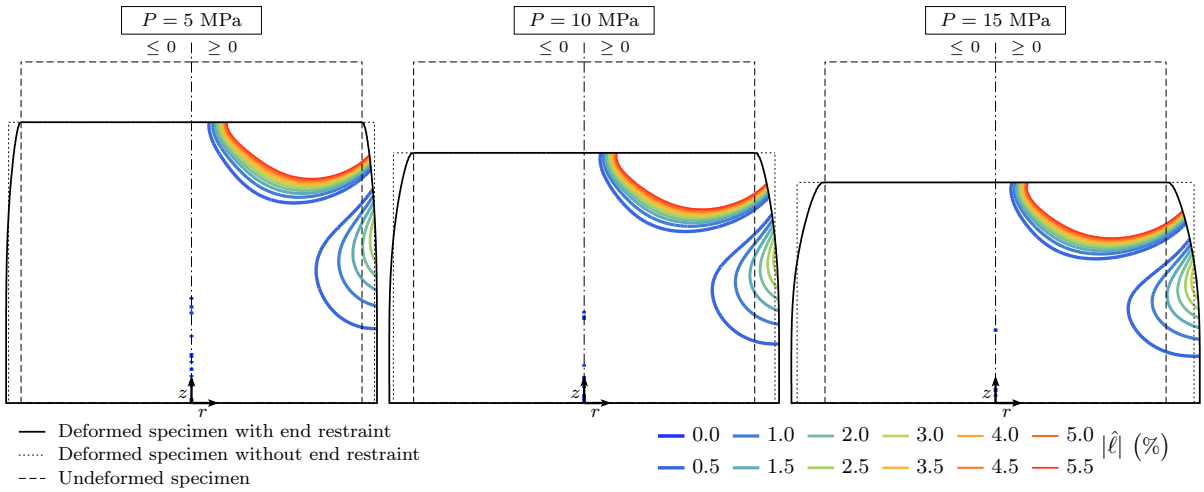

Fig. 16. Contour maps of the relative variation $\hat{\ell}$ for three confining pressures, with displacement scaling factor $A = 20$.

response in the ideal case. Fig. 17 shows the deviatoric stress $\bar{q}^\star$ (normalized by its value $\bar{q}^{\star\star}$, obtained for $\chi = 0$) as a function of the parameter χ which controls the effect of the intermediate principal stress by acting on the difference in material behavior between triaxial compression and triaxial extension. Depending on the value of the parameter χ, ranging from 0 to 1 ($\varrho(\theta) \in [0.5, 1]$), the dilatancy deviatoric stress $\bar{q}^\star$ decreases as χ increases, with a nonlinear behavior when χ approaches 1.

Regarding the case with end restraint, let us first consider the difference between the compression ($\bar{\ell} = -1$) and extension ($\bar{\ell} = 1$) tests without the effect of χ (i.e. $\chi = 0$ in both cases). Fig. 18 shows the stress-strain curves for both cases. Four observations can be drawn from these results. First, the stress-controlled compression test has qualitatively the same behavior as that observed in the previous strain-controlled tests. Second, the local and especially the global numerical measurements of the extension test are closer to the ideal case than those of the compression test. Third, the hybrid numerical measurements are very different from one another: the true dilatancy deviatoric stress ($\approx$ 17 MPa) is underestimated in the compression test ($\approx$ 11 MPa), while it is overestimated in the extension test ($\approx$ 20 MPa). Fourth, for both cases, the deviatoric behavior shows less difference with the ideal case than that observed with the strain-controlled tests, particularly in terms of local

measurements. This observation is consistent with the fact that the stress field within the specimen is, in this case, rather homogeneous in the central part of the specimen, as can be seen in Figs. 19-21 showing, for three values of χ, the contour maps of the relative variations $\hat{p}$, $\hat{q}$ and $\hat{\ell}$.

As can also be observed from those figures, besides the fact that in this case the specimen becomes hourglass-shaped as a consequence of end restraint, the stress distribution is clearly influenced by the value of χ as χ increases, i.e. Lode angle dependency increases, the heterogeneity of the invariants p and ℓ increases; the deviatoric stress q for its part seems to vary slightly with χ, in particular in the middle part of the specimen.

Unlike strain-controlled tests under high confining pressure, the major principal stress σ_1 within the specimen can become positive during the constant mean pressure tests even under high mean pressure as can be seen from Fig. 22 showing, for three times around $t^\star$, the contour maps of σ_1. The end restraint leads to the emergence of two tension zones ($\sigma_1 > 0$) that join during the test: one smaller which starts earlier in the test at the end corners of the specimen, and one larger which starts after the dilatancy onset at a distance of about $H/8$ from the end surface. Those zones could have an impact on the stress-strain curves, as in the case of the strain-controlled tests under low confining pressure. Fig. 23 shows an example of behavior obtained when activating the tension mechanism (with the same parameter Λ as that in Fig. 13). When compared to the case with $\Lambda = 0$ (see Fig. 18, $\bar{\ell} = 1$), differences can be observed mainly in the curve shapes after the dilatancy onset and in the hybrid numerical measurements; the local and the global numerical ones give nearly the same dilatancy deviatoric stress ($\approx$ 16 MPa). No significant differences are observed with regard to the deviatoric behavior.

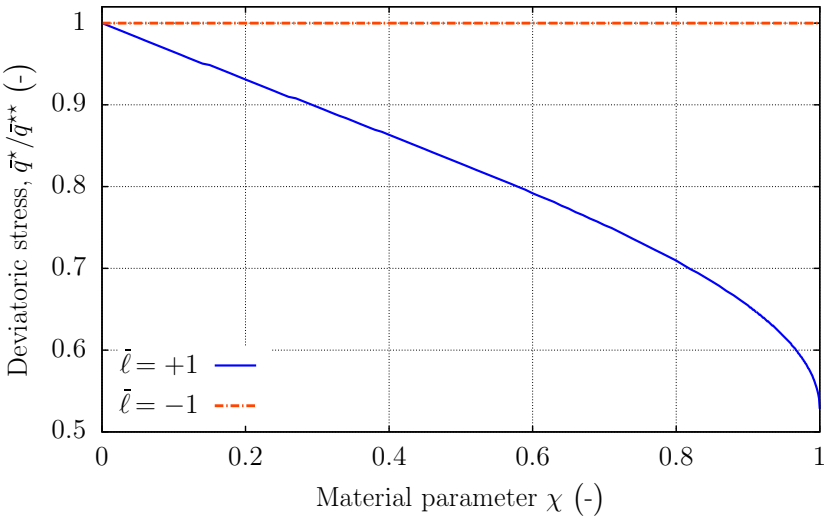

Fig. 17. Effect of the parameter χ on the dilatancy deviatoric stress in the ideal case.

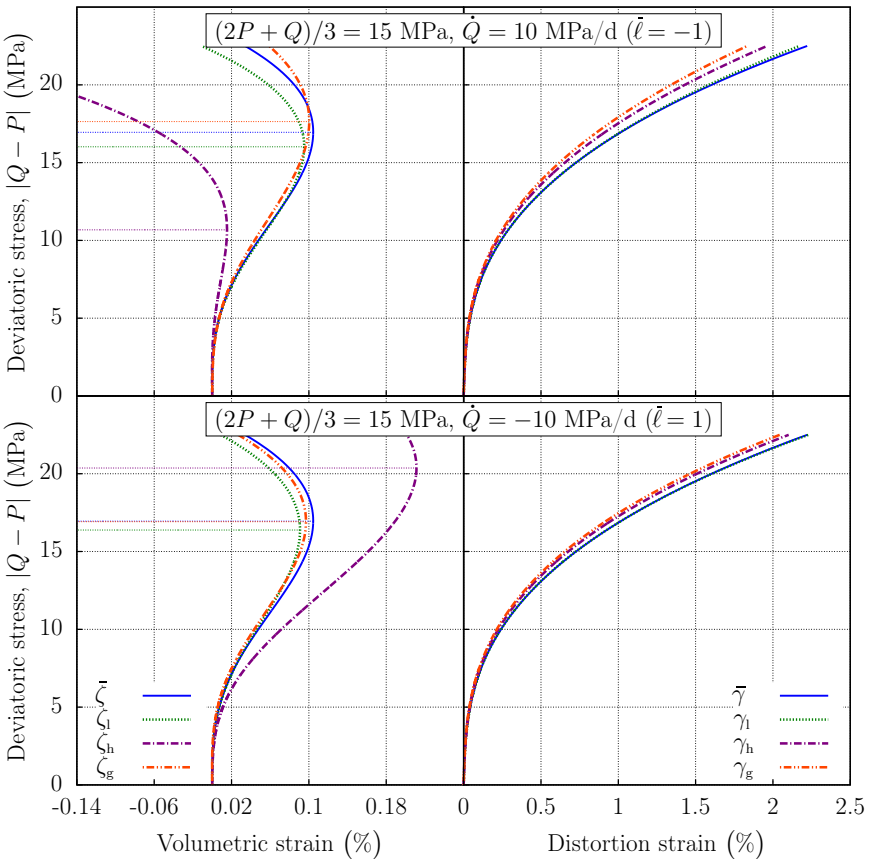

Fig. 18. Numerical stress-strain curves for a triaxial compression (top) and a triaxial extension (bottom) tests.

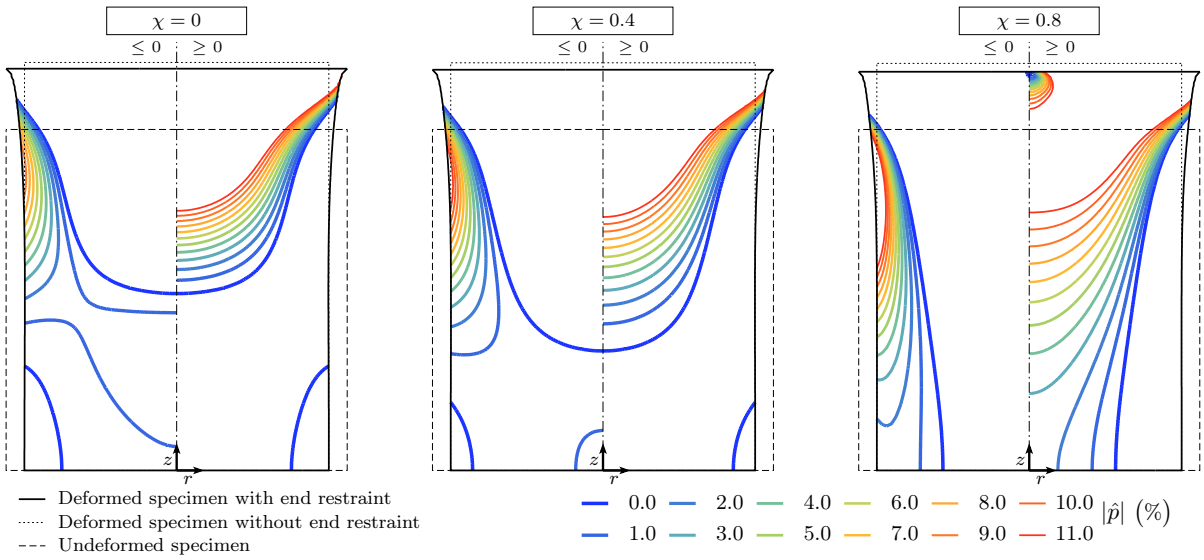

Fig. 19. Contour maps of the relative variation $\hat{p}$ for three values of χ, with displacement scaling factor $A = 20$.

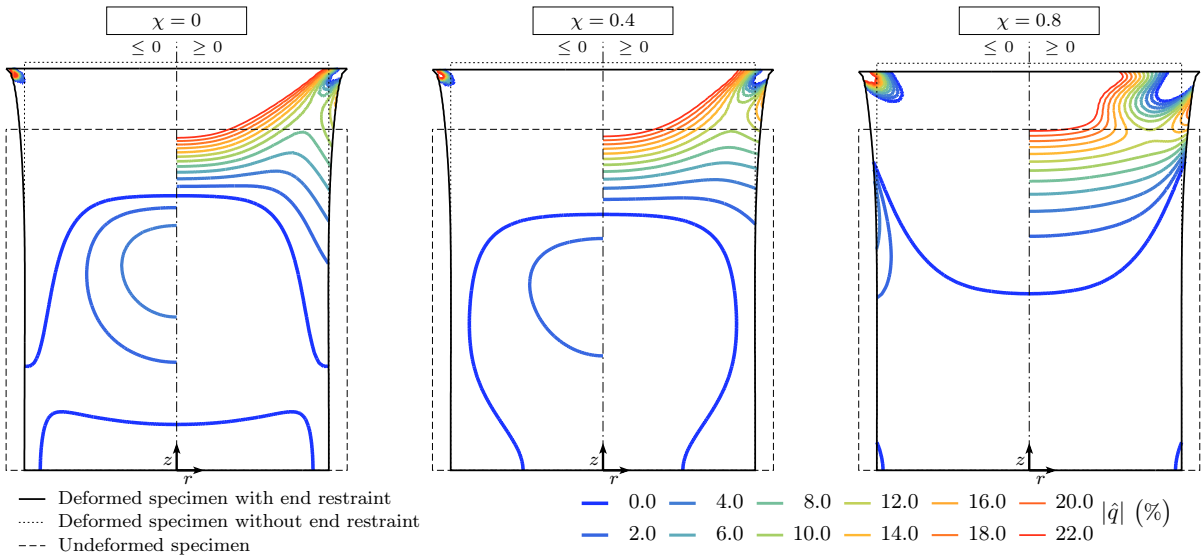

Fig. 20. Contour maps of the relative variation $\hat{q}$ for three values of χ, with displacement scaling factor $A = 20$.

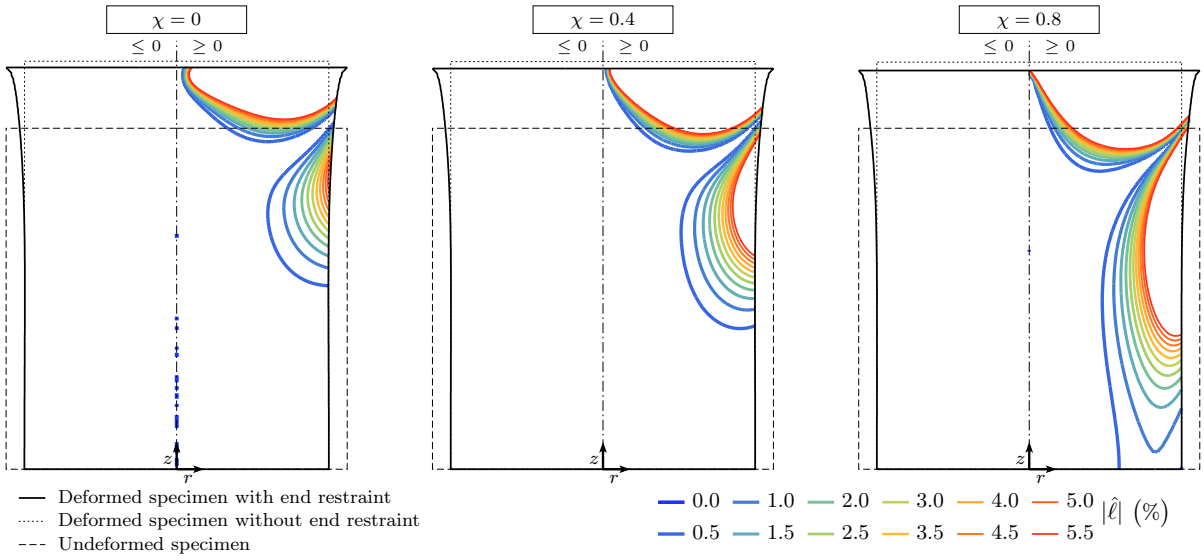

Fig. 21. Contour maps of the relative variation $\hat{\ell}$ for three values of χ, with displacement scaling factor $A = 20$.

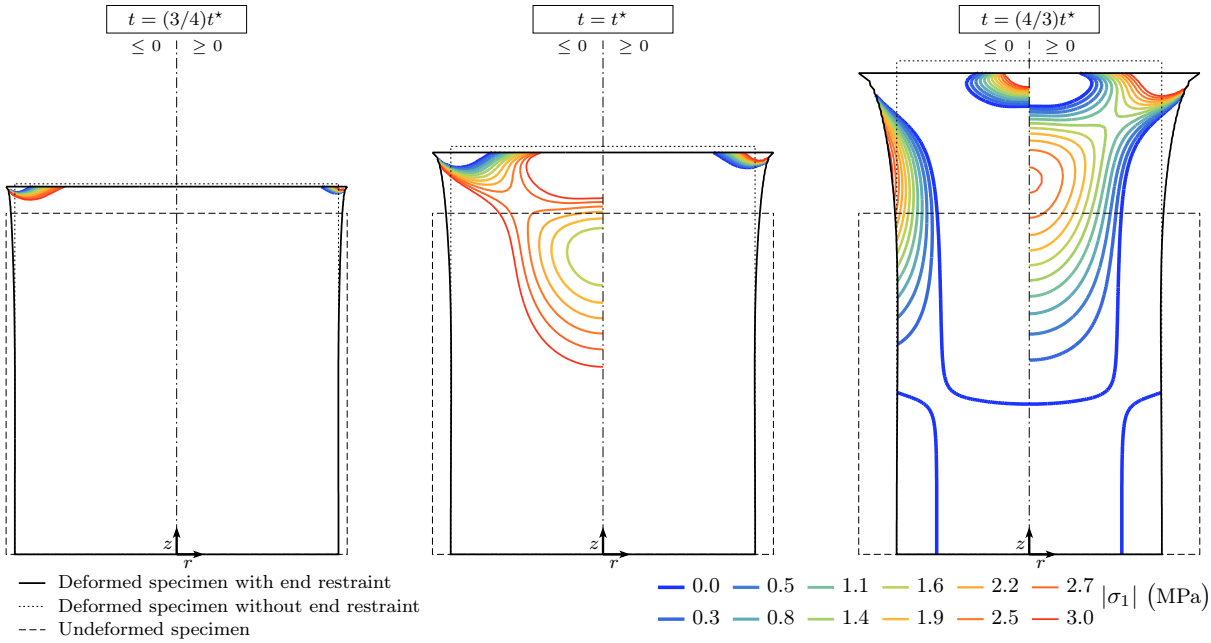

Fig. 22. Contour maps of the major principal stress σ_1 (tension positive) for three times around $t^\star$, with displacement scaling factor $A = 20$.

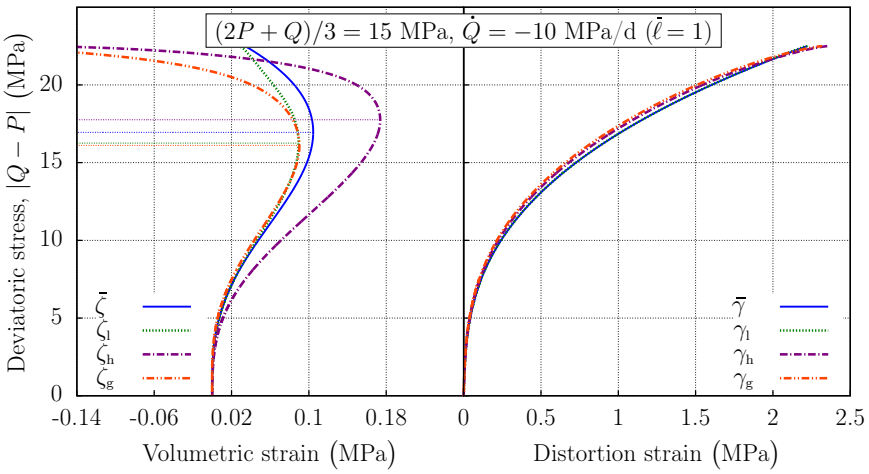

Fig. 23. Numerical stress-strain curves for a triaxial extension test, with tensile multiplier $\Lambda = 10^6$.

5.5. Summary of the main results

Taking the ideal case as a reference, several conclusions can be drawn:

(1) The difference between local and global measurements is less important than it experimentally appears. This may be interpreted, if we exclude the gauge dysfunctions, as the effects of other factors (specimen geometry, material heterogeneity, etc.) which were not investigated in this work.

(2) During compression tests, global measurements overestimate the dilatancy deviatoric stress, whereas local measurements underestimate it (error around 5%). In turn, hybrid measurements show a much greater deviation and underestimate it (error up to 50%).

(3) Strain- and stress-controlled compression tests show qualitatively the same behavior. The stress-controlled tests however show greater similarities between the ideal case and the local and global measurements for the case with end restraints (error under 5%). In turn, hybrid measurements still show large deviations (error around 35%).

(4) Under similar testing conditions, hybrid measurements from stress-controlled compression and extension tests underestimate and overestimate the dilatancy deviatoric stress, respectively.

(5) At the time corresponding to the dilatancy onset ($t^\star$), stress fields show less heterogeneities during stress-controlled tests than during strain-controlled ones. More precisely, during stress-controlled tests, a significant portion of the center of the specimen remains homogeneous. This explains the fact that for stress-controlled tests, local and global measurements are close to the ideal case. For high confining pressures (greater than 1 MPa in this study), stress field distributions are only slightly affected by the confining pressure and the loading rate levels, whereas they are significantly affected for low confining pressures.

(6) Tensile zones can appear during strain-controlled tests under low confining pressures as well as during stress-controlled tests under even high mean pressures. In the former case, these zones cause the dilatancy deviatoric stress to greatly decrease, whereas in the latter case they have no significant effects on the dilatancy onset.

(7) For homogeneous tests, the loading rate, confining pressure, and intermediate principal stress all had a significant impact on the volumetric strain. The dilatancy deviatoric stress increases with the loading rate and the confining pressure. It is lower under extension state of stress than under compression. Variations of parameter χ, which induces more or less difference between extension and compression, amplifies this effect: the greater the χ, the lower the dilatancy deviatoric stress.

(8) Few deviations are noted regarding the stress-strain curves associated with the deviatoric behavior; differences remain within the experimental error limits.

6. Conclusions

In this paper, the influence of the laboratory conditions on the dilatancy onset deduced from conventional triaxial tests was investigated experimentally and numerically. The experimental investigation consisted in a series of triaxial tests during which strains were measured both locally and globally. As for the numerical investigation, those triaxial tests were simulated under different laboratory conditions and with different end restraint effects.

The significant difference between the two experimental measurement techniques exhibited the issue with processing test data under the assumption of homogeneous stress and strain fields and using them to define an onset of dilatancy. It showed evidence of end effects that need to be taken into account. These observations were substantiated by the numerical investigation, which showed a difference between the predicted dilatancy deviatoric stress that can reach 50%.

The dilatancy deviatoric stress is more sensitive to end effects for strain- than for stress-controlled tests. In the former case, this sensitivity is caused by the significant heterogeneity of the stress field, as well as by the appearance of tensile zones for low confining pressures. Moreover, regardless of end effects, the dilatancy deviatoric stress depends on the loading rate: in the range of loadings commonly used for laboratory tests, it can greatly increase with the loading rate.

From all these considerations, it seems clear that the stress criteria based on the dilatancy onset should be used with great care and full knowledge of their limitations when introduced in structural design approaches as independent material thresholds. Even if the problem of measurement techniques is solved, the effect of the loading rates cannot be ignored, unless the actual ranges of the loading rates are very limited. The use of stand-alone rate-independent criteria in a wide range of loading rates seems therefore unsuitable and inconsistent with the rheological behavior of rock salt. A way to overcome this problem would be the use of a constitutive model, such as the one used in this paper that includes dilatancy at the constitutive level, and the definition of a design criterion such that $\dot{\zeta}_{\mathrm{vp}} = 0$. The advantage of such approach is that the inconsistency between the constitutive law and the design criterion is removed, particularly when the range of the loading rates is important as will be potentially the case for salt caverns within the energy transition context where high cycling rates are expected.

Conflicts of interest

The authors wish to confirm that there are no known conflicts of interest associated with this publication and there has been no significant financial support for this work that could

have influenced its outcome.

Acknowledgments

The authors would like to thank their colleagues Laura Blanco-Martín and Faouzi Hadj-Hassen, from MINES ParisTech, and Thierry You and Mehdi Karimi-Jafari, from Geostock, for their contributions.

Notations

Second-order tensors are denoted by two lines under the symbol, e.g. $\underline{\underline{a}}$. The second-order unit tensor is denoted by $\underline{\underline{1}}$. For a tensor $\underline{\underline{a}}$, $(\underline{\underline{a}})^{\mathrm{S}}$ is its symmetric part, $\mathrm{tr}(\underline{\underline{a}})$ is its trace, $\|\underline{\underline{a}}\| = \sqrt{\underline{\underline{a}} : \underline{\underline{a}}}$ is its norm and $\underline{\underline{a}}' = \underline{\underline{a}} - \mathrm{tr}(\underline{\underline{a}})\underline{\underline{1}}/3$ is its deviatoric part.

t Time (s)

$\underline{\underline{\sigma}}$ Cauchy stress tensor (Pa)

$p = -\mathrm{tr}(\underline{\underline{\sigma}})/3$ Hydrostatic component of $\underline{\underline{\sigma}}$ (Pa)

$q = \sqrt{3/2}\|\underline{\underline{\sigma}}'\|$ Deviatoric component of $\underline{\underline{\sigma}}$ (Pa)

$\ell = \sqrt{6}\,\mathrm{tr}(\underline{\underline{J}}^3) \in [-1, 1]$ Third invariant of $\underline{\underline{\sigma}}$

$\theta = \cos^{-1}\ell/3 \in [0, \pi/3]$ Lode angle (rad)

$\underline{\underline{I}}$, $\underline{\underline{J}}$, $\underline{\underline{K}}$ Orthonormal basis of the stress space

$\underline{\underline{\underline{N}}}^{\mathrm{c}}$, $\underline{\underline{\underline{N}}}^{\mathrm{t}}$ Deviatoric unit tensors

$\sigma_1 \geq \sigma_2 \geq \sigma_3$ Principal stresses (Pa)

$\varrho(\theta)$ Function defining the deviatoric cross-section

$\underline{\underline{\varepsilon}}_{\mathrm{vp}}$, $\underline{\underline{\varepsilon}}^{\mathrm{c}}_{\mathrm{vp}}$, $\underline{\underline{\varepsilon}}^{\mathrm{t}}_{\mathrm{vp}}$ Total, compressive and tensile viscoplastic strain tensors

ζ, γ Total volumetric and distortion strains

ζ_{vp}, γ_{vp} Viscoplastic volumetric and distortion strains

$\zeta^{\mathrm{c}}_{\mathrm{vp}}$, $\zeta^{\mathrm{t}}_{\mathrm{vp}}$ Compressive and tensile viscoplastic volumetric strains

$\gamma^{\mathrm{c}}_{\mathrm{vp}}$, $\gamma^{\mathrm{t}}_{\mathrm{vp}}$ Compressive and tensile viscoplastic distortion strains

λ Tensile viscoplastic strain

R_0 Initial specimen radius (m)

H_0 Initial specimen height (m)

$\mathcal{V}_0$ Initial specimen volume (m^3)

H Actual specimen height (m)

$\mathcal{V}$ Actual specimen volume (m^3)

$\tilde{R}$ Actual radius of the central part of the specimen (m)

$\tilde{V}$ Volume of the cylinder ($\tilde{R}$, H) (m^3)

$\varepsilon_H = -(H - H_0)/H_0$ Axial engineering

strain

$\varepsilon_{\tilde{R}} = (\tilde{R} - R_0)/R_0$ Radial engineering strain

ζ_l, ζ_h, ζ_g Local, hybrid and global volumetric strains

γ_l, γ_h, γ_g Local, hybrid and global distortion strains

P, Q Confining pressure and global axial stress during triaxial tests (Pa)

Subscripts and superscripts

l, h, g Local, hybrid, global

c, t Compression, tension

Special symbols

$\overline{\varphi}$ Function φ in the idealized behavior

$\hat{\varphi}$ Relative deviation of φ from the idealized behavior (%)

$t^\star$ Time corresponding to the dilatancy onset (s)

$\varphi^\star$ Function φ at the time $t^\star$

References

Al-Chalabi, M, Huang, C. Stress distribution within circular cylinders in compression. International Journal of Rock Mechanics and Mining Sciences & Geomechanics Abstracts 1974; 11(2):45–56.

Aubertin, M, Yahya, O. M. L, Julien, M. Modeling mixed hardening of alkali halides with a modified version of an internal state variables model. International Journal of Plasticity 1999; 15(10):1067–1088.

Bérest, P, Brouard, B, Feuga, B, Karimi-Jafari, M. The 1873 collapse of the Saint-Maximilien panel at the Varangéville salt mine. International Journal of Rock Mechanics and Mining Sciences 2008; 45(7):1025–1043.

Bigoni, D, Piccolroaz, A. Yield criteria for quasibrittle and frictional materials. International Journal of Solids and Structures 2004; 41(11):2855–2878.

Brace, W, Paulding, B, Scholz, C. Dilatancy in the fracture of crystalline rocks. Journal of Geophysical Research 1966; 71(16):3939–3953.

Brady, B. An exact solution to the radially end-constrained circular cylinder under triaxial loading. International Journal of Rock Mechanics and Mining Sciences & Geomechanics Abstracts 1971; 8(2):165–178.

Carol, I, Rizzi, E, Willam, K. On the formulation of anisotropic elastic degradation. ii. generalized pseudo-rankine model for tensile damage. International Journal of Solids and Structures 2001; 38(4):519–546.

Chaboche, J, Lesne, P, Marie, J. Phenomenological damage mechanics of brittle materials with description of

the unilateral damage effects. In: Bazant et al, Z (Ed.), Fracture and Damage in Quasibrittle Structures, Experiment, Modelling and Computer Analysis. E&FN Spon 1994.

Chan, K. S, Brodsky, N. S, Fossum, A. F, Bodner, S. R, Munson, D. E. Damage-induced nonassociated inelastic flow in rock salt. International Journal of Plasticity 1994; 10(6):623–642.

Chau, K, Wei, X. Finite solid circular cylinders subjected to arbitrary surface load. Part I - Analytic solution. International Journal of Solids and Structures 2000; 37(40):5707–5732.

Chemenda, A. I. Three-dimensional numerical modeling of hydrostatic tests of porous rocks in a triaxial cell. International Journal of Rock Mechanics and Mining Sciences 2015; 76:33–43.

Cipullo, A, White, W, Lee, I. K. Computer controlled volumetric strain measurements in metadolerite. Bulletin of the International Association of Engineering Geology 1985; 32:55–65.

Cristescu, N, Hunsche, U. Time effects in rock mechanics. Wiley New York 1998.

Cristescu, N. D. A general constitutive equation for transient and stationary creep of rock salt. International Journal of Rock Mechanics and Mining Sciences & Geomechanics Abstracts 1993; 30(2):125–140.

Crouch, S. L. Experimental determination of volumetric strain in failed rock. International Journal of Rock Mechanics and Mining Sciences & Geomechanics Abstracts 1970; 7(4):231–241.

DeVries, K, Callahan, G, Mellegard, K. Numerical simulations of natural gas storage caverns in bedded salt. In: The 40th US Symposium on Rock Mechanics (USRMS). American Rock Mechanics Association 2005.

DeVries, K. L, Mellegard, K. D. Effect of specimen preconditioning on salt dilation onset. In: SMRI Fall 2010 Technical Conference. Leipzig, Germany October 2010.

Fung, Y, Tong, P. Classical and Computational Solid Mechanics. Advanced Series in Engineering Science 2001.

Ghasemloonia, A, Butt, S. Feasibility study of underground salt caverns in Western Newfoundland: experimental and finite element investigation of creep-induced damage. Journal of Mining and Environment 2015; 6(2):205–224.

Heusermann, S, Rolfs, O, Schmidt, U. Nonlinear finite-element analysis of solution mined storage caverns in rock salt using the lubby2 constitutive model. Computers & structures 2003; 81(8-11):629–638.

Hou, Z. Mechanical and hydraulic behavior of rock salt in the excavation disturbed zone around underground facilities. International Journal of Rock Mechanics and Mining Sciences 2003; 40(5):725–738.

Hunsche, U, Hampel, A. Rock salt—the mechanical properties of the host rock material for a radioactive waste repository. Engineering geology 1999; 52(3-4):271–291.

Hunsche, U. E. Failure behaviour of rock salt around underground cavities. In: Proceedings of the 7th Symposium on Salt. Vol. 1 1993. pp. 59–65.

Ibsen, L. B, Lade, P. V. Effects of nonuniform stresses and strains on measured characteristic states. Tech. rep., Geotechnical Engineering Group 1999.

Ingraham, M. D, Broome, S. T, Bauer, S. J, Barrow, P. C, Flint, G. M. Geomechanical testing of bayou choctaw 102b core for spr analysis. Tech. Rep. SAND2014-1459, Sandia National Laboratories, Albuquerque, New Mexico 2014.

Jin, J, Cristescu, N. An elastic/viscoplastic model for transient creep of rock salt. International Journal of Plasticity 1998; 14(1-3):85–107.

Khaledi, K, Mahmoudi, E, Datcheva, M, Schanz, T. Stability and serviceability of underground energy storage caverns in rock salt subjected to mechanical cyclic loading. International Journal of Rock Mechanics and Mining Sciences 2016; 86:115–131.

Labaune, P, Rouabhi, A, Tijani, M, Blanco-Martín, L, You, T. Dilatancy criteria for salt cavern design: A comparison between stress-and strain-based approaches. Rock Mechanics and Rock Engineering 2018; 51(2):599–611.

Liyanapathirana, D. S, Carter, J, Airey, D. Numerical modeling of nonhomogeneous behavior of structured soils during triaxial tests. International Journal of Geomechanics 2005; 5(1):10–23.

Medina-Cetina, Z, Rechenmacher, A. Influence of boundary conditions, specimen geometry and material heterogeneity on model calibration from triaxial tests. International Journal for Numerical and Analytical Methods in Geomechanics 2010; 34(6):627–643.

Mellegard, K, DeVries, K, Callahan, G. Lode angle effects on the deformational properties of natural rock salt. In: The 40th US Symposium on Rock Mechanics (USRMS). American Rock Mechanics Association 2005.

Moghadam, S. N, Mirzabozorg, H, Noorzad, A. Modeling time-dependent behavior of gas caverns in rock salt considering creep, dilatancy and failure. Tunnelling and Underground Space Technology 2013; 33:171–185.

Moghadam, S. N, Nazokkar, K, Chalaturnyk, R. J, Mirzabozorg, H. Parametric assessment of salt cavern performance using a creep model describing dilatancy and failure. International Journal of Rock Mechanics and Mining Sciences 2015; 79:250–267.

Munson, D. E. Constitutive model of creep in rock salt applied to underground room closure. International Journal of Rock Mechanics and Mining Sciences 1997; 34(2):233–247.

Peng, S. Stresses within elastic circular cylinders loaded uniaxially and triaxially. International Journal of Rock Mechanics and Mining Sciences & Geomechanics Abstracts 1971; 8(5):399–432.

Popp, T, Minkley, W, Salzer, K, Schulze, O. Gas transport properties of rock salt–synoptic view. In: Mechanical Behavior of Salt VII. CRC Press/Balkema, Leiden 2012. pp. 143–153.

Popp, T, Wiedemann, M, Kansy, A, Pusch, G. Gas transport in dry rock salt–implications from laboratory investigations and field studies. In: The mechanical behavior of salt–understanding of THMC processes in salt. CRC Press 2017. pp. 31–40.

Sheng, D, Westerberg, B, Mattsson, H, Axelsson, K. Effects of end restraint and strain rate in triaxial tests.

Computers and Geotechnics 1997; 21(3):163–182.

Shilko, S. The role of friction in mechanical tests of materials. Journal of Friction and Wear 2002; 23(3):98–102.

Sobolik, S. R, Ehgartner, B. L. Analysis of the stability of large-diameter caverns for the strategic petroleum reserve. In: SMRI Spring 2011 Technical Conference. Galveston, Texas, USA April 2011.

Spiers, C, Peach, C, Brzesowsky, R. Long-term rheological and transport properties of dry and wet salt rocks: final report. Office for Official Publications of the European Communities 1989.

Staudtmeister, K, Rokahr, R. Rock mechanical design of storage caverns for natural gas in rock salt mass. International Journal of Rock Mechanics and Mining Sciences 1997; 34(3-4):300–e1.

Tijani, M. Zones de traction au cours d'essais de compression. In: 6th ISRM Congress. International Society for Rock Mechanics 1987.

Tijani, M. Contribution à l'étude thermomécanique des cavités réalisées par lessivage dans des formations géologiques salines. Habilitation à Diriger des Recherches, spécialité Sciences de l'Univers. Université Pierre et Marie Curie 2008.

Tijani, S. Short description of viplef code. In: Developments in geotechnical engineering. Vol. 79. Elsevier 1996. pp. 507–511.

Ulusay, R. The ISRM suggested methods for rock characterization, testing and monitoring: 2007-2014. Springer 2015.

Van Sambeek, L. L, Ratigan, J. L, Hansen, F. D. Dilatancy of rock salt in laboratory tests. International Journal of Rock Mechanics and Mining Sciences & Geomechanics Abstracts 1993; 30(7):735–738.

Wang, T, Ma, H, Shi, X, Yang, C, Zhang, N, Li, J, Ding, S, Daemen, J. Salt cavern gas storage in an ultra-deep formation in hubei, china. International Journal of Rock Mechanics and Mining Sciences 2018a; 102:57–70.

Wang, T, Yang, C, Chen, J, Daemen, J. Geomechanical investigation of roof failure of china's first gas storage salt cavern. Engineering Geology 2018b; 243:59–69.

Wang, T, Yang, C, Ma, H, Li, Y, Shi, X, Li, J, Daemen, J. Safety evaluation of salt cavern gas storage close to an old cavern. International Journal of Rock Mechanics and Mining Sciences 2016; 83:95–106.

Wei, X. X, Chau, K. T. Finite and transversely isotropic elastic cylinders under compression with end constraint induced by friction. International Journal of Solids and Structures 2009; 46(9):1953–1965.

Yang, C, Wang, T, Ma, H, Li, Y, Shi, X, Daemen, J. Feasibility analysis of using horizontal caverns for underground gas storage: A case study of Yunying salt district. Journal of Natural Gas Science and Engineering 2016; 36:252–266.